SLING-SHOT BUCKLING IN STACKED PIEZOELECTRIC STRUCTURES

By

MICHAEL PAVLOU

A thesis submitted to the

Graduate School-New Brunswick

Rutgers, The State University of New Jersey

in partial fulfillment of the requirements

for the degree of

Master of Science

Graduate Program in Mechanical & Aerospace Engineering

written under the direction of

Dr. William J. Bottega

and approved by

____

____

____

New Brunswick, New Jersey

January 2014

ABSTRACT OF THE THESIS

Sling-Shot Buckling in Stacked Piezoelectric Structures

by MICHAEL J. PAVLOU

Thesis Director:

Dr. William J. Bottega

A stacked structure consisting of two beam-plates, each being a different piezoelectric material, subject to a uniformly increasing electric field is analyzed. One beam-plate is perfectly adhered over the central portion of the other. We consider the limiting boundary conditions for the bottom layer, the baseplate: clamped-fixed and hinged-fixed boundaries. A quasi-static analysis is performed, in which a geometrically nonlinear strain-displacement relation is incorporated to account for infinitesimal strain, while allowing for moderate rotation of the structure. The strain energy of the stacked structure is formulated, and the governing equations, constitutive relations, and boundary and matching conditions are derived self-consistently after invoking the Theorem of Stationary Potential Energy. Stability is assessed through evaluation of the second variation of the PE under perturbation. A closed form analytical solution is obtained, and numerical simulations based on these solutions are presented. It is shown that, for certain combinations of piezoelectric materials and orientations of the applied increasing electric field, the structure will exhibit sling-shot buckling—an instability where the orientation of the deflection of the structure will dynamically change when a critical electric field and critical membrane force are reached. These critical values are identified from the analytical equations. A parameter study shows how the critical values depend on various geometric and material properties of the structure.

Acknowledgment

I would like to express my thanks and appreciation to all those who helped make the writing of this thesis possible. There are surely too many people to name them all.

Foremost, I would like to thank my advisor, Dr. William J. Bottega. Without his guidance and teaching, this work would not exist. Dr. Bottega has served as an advisor and mentor, helping and encouraging my development as a student and as a person at every step along the way. For this I am eternally grateful.

I would also like to thank my mother, Barbara Jean, and my father, William. Without their hard work, higher education would not have been a possibility for me. The two of them have never stopped encouraging my intellectual curiosity, and have always supported me entirely in all of my endeavors.

In addition, I express sincere thanks to the members of my committee: Dr. Haim Baruh and Dr. Kimberly Cook-Chennault. Their input has helped enrich this thesis. Also, thanks to Cynthia Cartegna, whose help with deadlines, forms, and in general, keeping me on track could not be understated.

I would also like to specifically thank Andrew Pavlou, Bill Pavlou, Amber McGoff, Joseph Lakawicz, and Peinan Ge, who have all helped greatly in their own ways.

Contents

List of Figures

1 Introduction

1.1 Motivation

Piezoelectric materials are widely used in a number of engineering applications. At the present time, there exists a plethora of applications for these materials, and new applications are being discovered at an accelerating rate. Piezoelectric materials are commonly used as actuators in mechanical systems, either to constrain motion or to induce motion. For example, they are often adhered to thin-walled structures in order to reduce deflections by a specific amount. Conversely, they can be made to increase the deflection by a specified amount. Another common application of piezoelectric materials is their usage in transducers, which convert electrical to mechanical energy or mechanical to electrical energy, depending on the application.

In what follows, a certain stacked piezoelectric structure is presented where upon application of a uniform external electric field, the structure deflects in one direction until a critical electric field is reached. At this point, the orientation of the deflection dynamically swings to the opposite sense, and the structure continues to deflect in the opposite direction as the electric field increases. This type of instability was first discovered by Karlsson and Bottega [4] for non-piezoelectric structures of this same geometry subjected to a uniformly increasing temperature field, and appropriately named "sling-shot buckling."

Systematic understanding of this phenomenon for piezoelectric materials is of great importance. This type of instability may need to be avoided in a piezoelectric device, so its origins must be understood. Conversely, this type of instability can be utilized in a productive manner. For example, one can make a piezoelectric device that regulates electric current in such a manner that when the critical electric field that induces sling-shot buckling is reached, the structure will deflect in the opposite sense, hitting a sensor that stops increasing the electric field. Also, as will be seen later, as the electric field increases after buckling, the structure becomes stiffer, monotonically. Thus, a device could be created that monitors and regulates the internal stress of a constrained structure.

1.2 Survey of Relevant Literature

1.2.1 Buckling

Since the thesis concerns the extension of the phenomenon of sling-shot buckling from a problem of a temperature field increase to that of an increasing electric field, it is instructive to fully understand the nature of buckling of stacked structures, as induced by thermal loading. Before delving into thermo-mechanically driven buckling, it is necessary to first present a survey of simpler mechanical buckling modes of stacked structures. This will shed some light onto the interesting dynamic nature of sling-shot buckling.

Buckling of Stacked Structures Due to Mechanical Loading

- **Bifurcation Buckling and "Asymptotic Buckling"**

The simplest, and most well-known type of buckling observed in structures is the classical Euler-type bifurcation buckling. Euler, in his 1757 work, derived the formula for the maximum allowable compressive axial load applied to an ideal beam-column before the beam-column became unstable. He noted that at a critical load the equilibrium configuration becomes unstable, and that any subsequent type of loading will result in the equilibrium solution bifurcating. The structure will then follow one of the two bifurcating paths depending on which direction it is initially favoring (usually due to some initial curvature or a defect in the structure).

We now consider the beam to be a stacked structure: one where we have a second layer perfectly adhered above the central portion of the original beam. The neutral axis of the stacked structure is moved up, which in the context of buckling orientation analysis is equivalent to giving the structure a pre-determined influence. Thus, a bending moment will develop when a compressive axial load is applied. Consequently, the load-displacement curve will asymptotically approach the bifurcating solution it is pre-influenced to lean towards. This is known as "asymptotic buckling." See Figures 1 and 2.

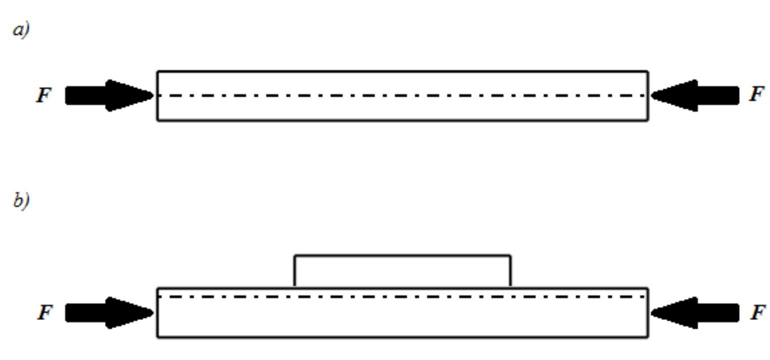

Figure 1: (a) A regular Euler-type beam-column subjected to a compressive axial load. (b) A stacked structure subjected to the same load as in (a).

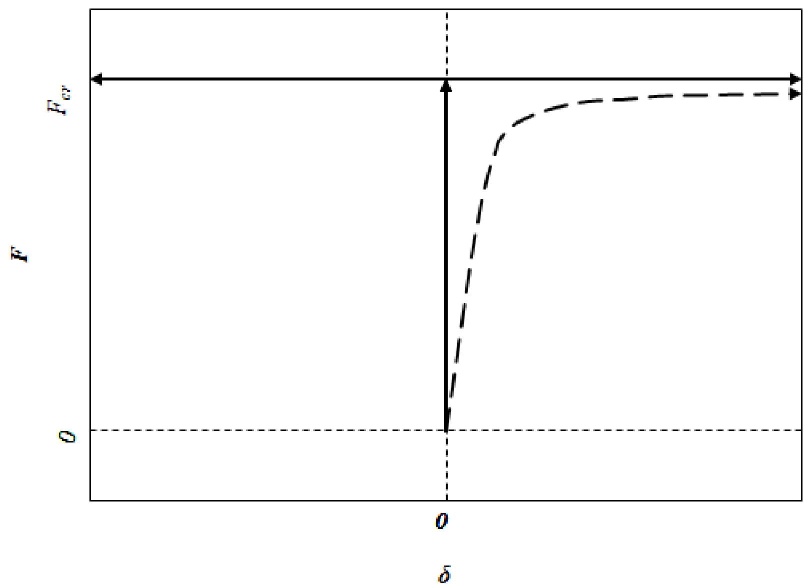

Figure 2: Load Deflection Curves. The solid lines represent the ideal beam-column, while the dashed lines are the path for the stacked structure.

Euler's formula for buckling arose from considering the geometrically nonlinear terms in relating strain and deflection. It is apparent that buckling can only be predicted when we allow for moderate rotations of the cross-sections of the beams.

- **Snap-Through Buckling**

Another important type of buckling is snap-through buckling (and its counterpart snap-back buckling). Simply stated, snap-through buckling is an instability where a structure with initial concave curvature is subjected to an increasing load, directed toward the center of curvature, until a critical value is reached. (See Figure 3.) At this point, an increase in deflection means a decrease in load. Since, however, the load is prescribed and will not decrease, the structure will settle upon a new equilibrium position associated with the opposite orientation of curvature. (See Figure 4.) It will "snap-through" the straight configuration and deflect in the opposite sense. This type of instability is often referred to as "oil canning," as this phenomenon is exploited in the design of old oil cans. They were designed with a shallow dome on the base. When one pressed down on the dome, it would snap through and the volume in the can would decrease as oil was released out of the nozzle. Upon releasing the force, the dome snaps back into its original configuration as air comes back into the can stopping the flow of oil.

Timoshenko presents an overview of snap-through and snap-back buckling in his 1961 text on elastic stability [23], where he refers to these instabilities as "the phenomenon of reversal of deflections."

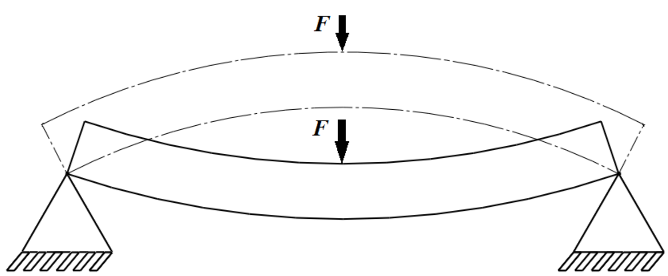

Figure 3: Physical Situation Corresponding to Snap-Through Buckling.

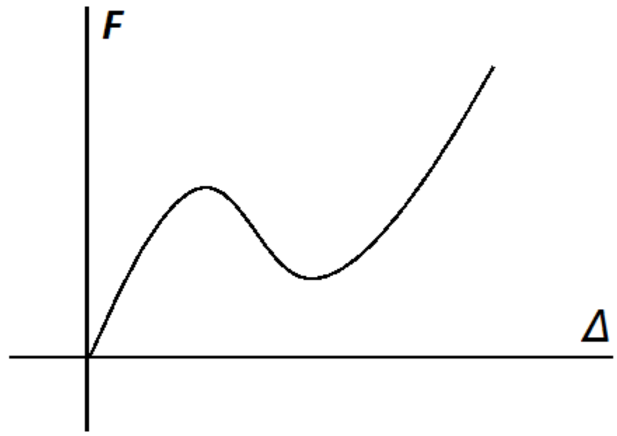

Figure 4: Load-Deflection Curve: Snap-Through Buckling.

It was later noted by Rutgerson and Bottega [15] that for shallow shells, snap-through buckling occurs below and often well below the previously known limit point. This assessment is based on an equilibrium stability argument that requires the second variation of the total potential energy of the structure to remain positive definite for stable configurations.

Buckling of Stacked Structures Due to Thermo-Mechanical Loading

We are not only concerned with understanding how buckling occurs when the driving force is purely mechanical, but also how buckling is influenced by an eigenstress. Specifically, the thesis is concerned with an electro-mechanical eignenstress, which is mathematically similar to thermo-mechanical loading. Timonshenko [22], in his 1925 work, studied the thermo-mechanical response of bi-metal thermostats. He was able to induce snap-through buckling of the structure under appropriate heating conditions. Reversibly, Timonshenko found the opposite effect of "snap-back" when the heated structure was cooled in a similar manner–this time at a lower temperature than the snap-through.

His work was furthered when in 1944, Wahl [25] was able to induce the same type of buckling in a Valverde thermostat. This is a similar configuration to Timoshenko's bi-metal strip, except that it consists of three-layers, each of which were considered to be pre-stressed.

It is apparent from these analyses that buckling instabilities are largely a function of geometry. The same geometrically nonlinear assumptions are made for the structures to be considered here, and it is revealed that the nature of the instability depends on the geometry of the configuration.

More recent research advances have been made concerning the behavior of thermo-mechanically loaded stacked structures. This area of research has been mainly motivated by the implementation of such structures as means of repair for aircraft and spacecraft. These layered structures are exposed to strong temperature fields as well as large temperature gradients. Thus, a great deal of the available literature is focused on debonding between the layers, which is not of concern to the present study. However a systematic approach to finding the overall composite properties of a layered plate under thermal loading is addressed by Tauchert [18], in his 1991 paper. Work by Noor and Burton from 1992 [12] and Noor and Peters in 1992 [13] addresses similar concerns but also deals with the issue of stability of the composite structure. Of course, much more progress has been made by countless others in the field of thermal buckling analysis, including Stavsky in 1975 [16], Leissa in 1987 [8], Thangaratnam et al. in 1989 [19], Sun and Hsu in 1990 [17], and Librescu and Souza (1993) [9].

- **Sling-Shot Buckling**

As previously discussed, sling-shot buckling was first discovered by Karlsson and Bottega (2000) [4]. They studied the problem of a stacked structure subject to a uniformly increasing thermal load. In the cases of interest to us, the structure was fixed at its ends from in-plane translation. It was found that when the two layers had different thermal expansion properties, an effective thermal bending moment acts on the edge of the patch. This moment opposes the mechanical moment created by the raised neutral axis of the structure (much like previously discussed for bifurcation of stacked structures). They identified a critical temperature and a critical membrane force, which predict the instant that the thermal moment overcomes the purely mechanical moment, and shifts the direction of deflection. Karlsson and Bottega [5] furthered their study of this structure when they considered cooling of the structure, as opposed to heating it. It was observed that the response of the structure was dramatically influenced by the in-plane displacement boundary conditions, but much less affected by the rotational edge conditions. This theory was extended from just plates to layered shell segments as well in the 2002 article by Rutgerson and Bottega [14]. A concise unified review of this phenomenon was given by Bottega (2006) [1].

Electro-Mechanical Buckling

There also exists much literature focused on the buckling of piezoelectric materials. The majority of this work focuses on adding piezoelectric materials to an existing structure with the aim of stiffening the overall structure. Heavily cited is the work of Meressi and Paden (1993) [11]. They studied the effects of adding piezoelectric actuators to thin beams in order to be able to control the buckling characteristics of the beam. Similar work of note includes that of Thompson and Loughlan (1995) [20] for composite column strips.

Among other more recent work is that of Varelis and Saravanos (2004) [24]. This paper studies the pre-buckling and postbuckling response of composite laminates with piezoelectric sensors and actuators adhered to the system. In addition, scenarios were introduced that would help palliate buckling of the structure, in a comparable fashion to that of Meressi and Paden.

1.2.2 The Piezoelectric Effect

So far, many statements have been made in regards to considering buckling of piezoelectric composites. However, we have not yet defined the concept of piezoelectricity. It is important to understand the piezoelectric effect from first principles so that we can appropriately apply this effect to layered structures.

Basic Principles and Discovery

It has long been observed that certain materials exhibit electromechanical coupling. That is, these materials deform mechanically when placed in an electric field, and conversely become electrically polarized when mechanical loads are applied. Quantitative analysis was first done on these electroelastic materials by brothers Pierre and Jacques Curie in 1880. They confirmed that when compressed, certain materials showed positive and negative charges on portions of their surface. The landmark conclusion of these experiments was the magnitude of the charges was directly proportional to the applied load. The Curie brothers were also able to give the first description of what type of crystal structures will lend themselves to this property. Since the discovery of piezoelectricity, a complete list of lattice structures with the ability to exhibit the piezoelectric effect has been compiled.

The Curie discovery tells only half of the story, however. They discovered what is referred to as the *direct piezoelectric effect*. Again, this is when a structure becomes polarized when a mechanical load is applied. The following year (1881), Gabriel Lippmann [10] mathematically showed the reversibility of this effect from a thermodynamics viewpoint, and essentially completed the theory of piezoelectricity. Lippman noted that when placed in a prescribed electric field, these structures will experience mechanical deformation. Lippmann also realized that the same proportionality constant between the applied field and the subsequent deformation was the same as observed in the direct piezoelectric effect. The effect discovered by Lippmann is what is now known universally as the *converse piezoelectric effect*.

3-D Piezoelectric Theory

The term piezoelectricity was first introduced into the vernacular by G.W. Hankel not long after its discovery, and has since gained universal acceptance. Piezoelectricity, in its strict modern definition, refers only to the linear theory or electromechanical coupling. The nonlinear extension of this phenomenon is called more generally the nonlinear theory of electroelasticity [26].

We present here the equations of motion and charge inside the body for the nonlinear theory of electroelasticity as derived in the text by Yang [26]:

$$K_{Lk,L} + \rho_0 f_k = \rho_0 \ddot{y}_k, \tag{1a}$$

$$\mathcal{D}_{K,K} = \rho_E, \tag{1b}$$

with constitutive relations:

$$K_{Lj} = y_{j,K}\rho_0 \frac{\partial \psi}{\partial S_{KL}} + JX_{L,i}\varepsilon_0 (E_i E_j - \frac{1}{2} E_k E_k \delta_{ij}), \tag{2a}$$

$$\mathcal{D}_K = \varepsilon_0 J C^{-1}_{KL} \mathcal{E}_L - \rho_0 \frac{\partial \psi}{\partial \mathcal{E}_K}, \tag{2b}$$

where K_{Lk} is the Piola stress tensor, ρ_0 is the reference mass density of the structure, f_k is an applied body force per unit of reference mass, y_k refers to the present position vector of a material point, $\mathcal{D}_K$ is the reference electric displacement vector, ρ_E is the free charge density per unit of reference volume, ψ is the free energy per unit mass, S_{KL} is the finite strain tensor, $J = det(y_{k,K})$ is the Jacobian of the deformation, $X_{L,i}$ is the inverse deformation gradient, ε_0 is the permittivity of free space, E_i is the electric field, $C^{-1}_{KL} = X_{K,k}X_{L,k}$ is the inverse deformation tensor, δ_{ij} is the Kronecker delta, and an overdot signifies differentiation with respect to time. In this notation, capitalized subscripts refer to properties of the undeformed structure, while those with lowercase subscripts are taken to be current properties of the deformed structure.

This theory applies for finite deformations, and is always applicable. However, since we are to only consider infinitesimal deformation of structures in our analysis, we are more interested in the linear theory of piezoelectricity. In his 1969 monograph, Tiersten [21] derives the linear form of the electroelastic equations.

$$c_{ijkl}u_{k,li} + e_{kij}\psi_{,ki} = \rho\ddot{u}_j, \tag{3a}$$

$$e_{ikl}u_{k,li} - \varepsilon_{ik}\psi_{,ki} = 0, \tag{3b}$$

where the constitutive equations have already been accounted for. Here, c_{ijkl} is the elasticity tensor, u_k is the displacement vector of a material point, e_{kij} refers to the piezoelectric constant tensor, ψ is the free energy per unit mass, ρ is the mass density, and ε_{ik} is the dielectric constant tensor. Of great concern for our purposes are the constitutive relations, specifically the one that relates the strain due to the piezoelectric effect to the overall stress of the body. The constitutive relations are as follows:

$$\sigma_{ij} = c_{ijkl}S_{kl} - e_{kij}E_k, \tag{4a}$$

$$\mathcal{D}_i = e_{ikl}S_{kl} + \varepsilon_{ik}E_k, \tag{4b}$$

where σ_{ij} is the Cauchy stress tensor, S_{kl} is the overall infinitesimal strain tensor, E_k is the electric field, and $\mathcal{D}_i$ is the electric displacement vector.

Reduced Equations for Beam Theory

It is apparent from the form of the above equations that the piezoelectric effect is inherently a three-dimensional phenomenon. The structures that we will analyze are assumed to be beams in a state of plane stress or beam-plates in a state of plane strain. We will be using a modified version of Euler-Bernoulli beam equations that will account for moderate rotations. In keeping with beam theory, we reduce the problem from a physically three-dimensional one to a mathematically one-dimensional problem. The assumptions are that due to the geometry of the structure, all stress components other than the normal axial and transverse shear components will vanish. To make quantitative statements about the forms of our equations, it is best to set up a coordinate system at this point. We will say that the beam lies in the x-y (1-2) plane and is subjected to deflections in the z-direction (3-direction). Thus, all stress components except for σ_{xx} (σ_{11}) and σ_{xz} (σ_{13}) vanish. However, $S_{13} = 0$, as transverse shear deformation is neglected. The constitutive relations then become:

$$\sigma_{11} = c_{1111} S_{11} - e_{311} E_3, \tag{5a}$$

$$\mathcal{D}_1 = e_{111} S_{11} + \varepsilon_{13} E_3, \tag{5b}$$

when the structures are poled in the 3-direction, and the electric field is applied in the 3-direction, which is a very common setup for piezoelectric structures.

We will also explore the case where the piezoelectric materials are poled in the 1-direction, along with an electric field applied in the 1-direction. The constitutive equations then become:

$$\sigma_{11} = c_{1111} S_{11} - e_{111} E_1, \tag{6a}$$

$$\mathcal{D}_1 = e_{111} S_{11} + \varepsilon_{11} E_1, \tag{6b}$$

We will use these equations in the second chapter to formally derive the equations of motion for our structures.

1.3 Thesis Outline

There are five chapters to this thesis. The first one being the introduction; it sets the groundwork for the problem to be studied and systematically develops the tools necessary to perform a meaningful analysis. The second chapter formally describes the structure. First, the geometry is established and kinematic relations are defined. Stiffness parameters are then identified. All variables and equations are normalized, as the total strain energy of the structure is formulated. From here, the constitutive equations, and boundary and matching conditions are found in a self-consistent manner using the calculus of variations. Finally, since we have a mixed formulation in terms of transverse displacement and membrane force, compatibility of the displacement field is ensured as an integrability condition is developed. In the third chapter, the governing equations are solved analytically for the transverse displacement of the structure, as the appropriate boundary and matching conditions are applied. The physical interpretations of the nature of the solution forms are analyzed, and the stability of these solutions is assessed. The fourth chapter presents the results of numerical simulations based on the analytic solutions previously derived. Interpretation of the load-deflection paths sheds insight into the nature of the instabilities. A parameter study is also presented based on the material properties of actual materials. Finally conclusions based on the results are drawn in the fifth chapter. Possible areas of future relevant research are addressed here, as well. The complete list of references is then included. The final section is the Appendix, which includes the codes used for the numerical simulations (written in MATLAB syntax).

2 Problem Formulation

2.1 Geometry

The configuration under consideration consists of a flat thin baseplate of normalized half-span length $L \equiv 1$ with a secondary layer of half-span $L_p < 1$ perfectly bonded on top of the baseplate. Symmetric deformations will be assumed, and thus, only half the body need be analyzed. The configuration consists of two regions: one with the two layers perfectly bonded, and one with just the baseplate. The non-dimensional path coordinate x begins at the center-span of the structure, and runs along the upper surface of the baseplate, which is defined as the reference surface. The first region, the one with two layers, is defined as $S_1 : x \in [0, L_p]$, while the region with just the baseplate is $S_2 : x \in [L_p, 1]$. The non-dimensional z-coordinate originates at the interface between the two layers—known as the reference surface—and is positive downward. The non-dimensional height of the baseplate is denoted by h_b, while that of secondary layer is h_p. In keeping with beam theory, it is assumed that $h_b, h_p \ll L$. See Figure 5. The model describes the two layers as beams (plane stress) or as infinite plates (plane strain).

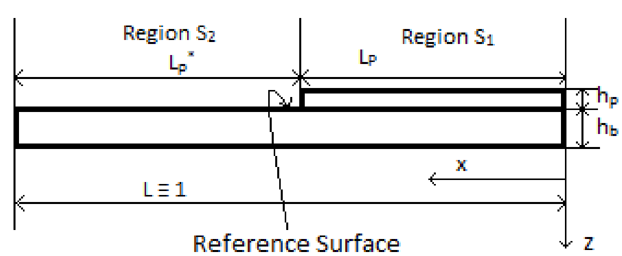

Figure 5: Non-dimensional Half-Span of Structure.

Both layers are composed of a distinct homogeneous material, which exhibits piezoelectric behavior. The evolution and behavior of this system when placed in a uniformly increasing electric field is analyzed. Moreover, the poling direction of these piezoelectric beam-plates is assumed to be in the same direction as the applied electric field. A quasi-static analysis is performed as the electric field increases uniformly.

Two different limiting boundary conditions are analyzed for this situation: clamped-fixed boundaries and hinged-fixed boundaries. See Figure 7. For a clamped-fixed boundary, the structure is constrained from axial displacement, and the entire boundary is fixed, prohibiting rotation at the boundary. For a hinged-fixed boundary, we mean that, again, the structure is restricted from displacing in the axial direction, but is bounded only at one point (the centroid of the baseplate). Hence, axial displacement is only zero at this one point, and the edge is free to rotate about that point.

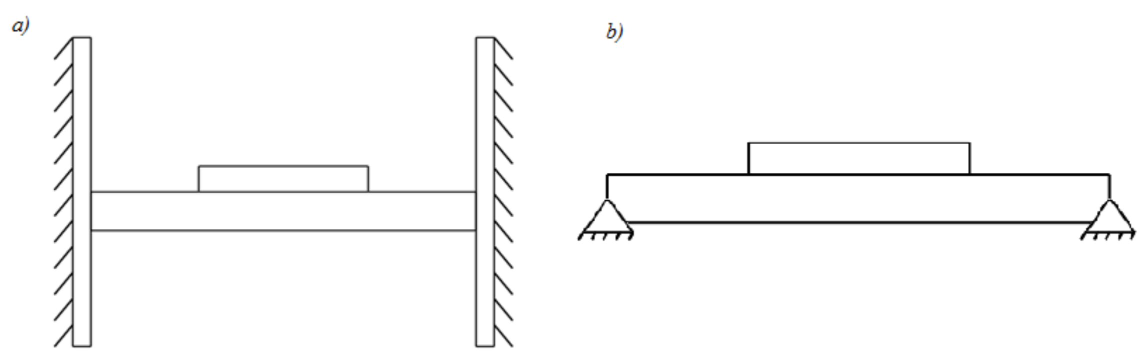

Figure 6: a) Layered Beam-Plate with Clamped-Fixed Boundaries. b) Layered Beam-Plate with Hinged-Fixed Boundaries.

2.2 Kinematic Relations

A geometrically nonlinear strain-displacement relation that accounts for infinitesimal strain and moderate rotation is employed. Here, u and w represent axial and transverse displacements, respectively. As stated earlier, u is taken as positive away from the center-span, and w is taken as positive downwards. The strain-displacement relations for either the baseplate or the secondary layer are:

$$e_\alpha = \frac{\partial u_\alpha}{\partial x} + \frac{1}{2}(\frac{\partial w_\alpha}{\partial x})^2 \quad \text{for } \alpha = b, p, \tag{7}$$

where e is the measure of strain.

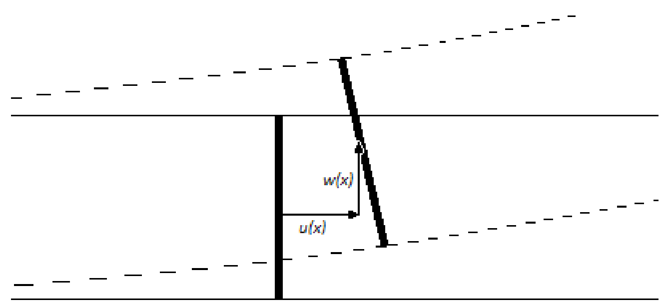

Figure 7: Differential element accounting for small strain and moderate rotation.

In addition to strain-displacement relations, the change in curvature, κ, is used, and is approximated in the following way:

$$\kappa_\alpha = \frac{w''_\alpha}{[1 + (w'_\alpha)^2]^{\frac{3}{2}}} \approx w''_\alpha \quad \text{for } \alpha = b, p, \tag{8}$$

where $'$ indicates differentiation with respect to the x-coordinate, as the only independent spatial variable that u and w depend on is x.

At this point, it is instructive to take these properties for the individual layers and extend them to the bonded region S_1 as one composite structure. To this end, Kirchhoff's hypothesis is employed to obtain the strain contribution from each layer at the reference surface by the following relations:

$$e_b^* = e + \frac{1}{2}h_b\kappa_b, \tag{9a}$$

$$e_p^* = e - \frac{1}{2}h_p\kappa_p, \tag{9b}$$

where * indicates the quantity is being evaluated at the reference surface.

It is also important to know the curvature at the reference surface. Since the assumption has already been made that the x-coordinate is the only independent spatial variable that transverse displacement depends upon, w does not vary through the thickness. Thus, curvature changes do not vary through the thickness, either. Hence,

$$\kappa_b = \kappa_p = \kappa^* \quad \text{in } S_1 \tag{10}$$

2.3 Material Stiffnesses of the Stacked Structure

With the geometry of the problem now defined, attention is shifted towards the relevant stiffness properties of the system. It is apparent from the model that bending energy and membrane strain energy will be the main modes of energy storage. Thus, we must quantify the bending stiffness and membrane stiffness for each layer.

In the case of plane stress, the bending stiffness parameters for the baseplate and the adhered layer are, respectively:

$$D_b = \frac{1}{12} E_b b_b h_b^3, \tag{11a}$$

$$D_p = \frac{1}{12} E_p b_p h_p^3. \tag{11b}$$

where E_b and E_p are Young's Modulus for each layer, and b_b and b_p are the width of each layer, respectively. It is assumed that in all cases $b_b = b_p$. Likewise, the membrane stiffness parameters for each layer are, respectively:

$$C_b = E_b b_b h_b, \tag{12a}$$

$$C_p = E_p b_p h_p. \tag{12b}$$

When plane strain is considered, the bending and membrane stiffnesses become:

$$D_b = \frac{1}{12} \frac{E_b}{1 - \nu_b^2} h_b^3, \tag{13a}$$

$$D_p = \frac{1}{12} \frac{E_p}{1 - \nu_p^2} h_p^3, \tag{13b}$$

$$C_b = \frac{E_b}{1 - \nu_b^2} h_b, \tag{13c}$$

$$C_p = \frac{E_p}{1 - \nu_p^2} h_p. \tag{13d}$$

where ν_b and ν_p represent Poisson's ratio for each layer, respectively.

2.4 Normalization of Parameters

Until this point, we have been considering dimensional values for all parameters stated. From this point forward, dimensional parameters are always denoted by an overbar, while those parameters without an overbar are normalized. This notation is used for convenience sake, as the problem will be analyzed in non-dimensional form. All length scales are normalized with respect to the dimensional half-span $\bar{L}$, of the baseplate. Hence, the normalized x-coordinate is defined as:

$$x = \frac{\bar{x}}{\bar{L}}. \tag{14}$$

This in turn causes the axial and transverse displacements, respectively, to be normalized in the following fashion:

$$u(x,z) = \frac{\bar{u}(\bar{x},\bar{z})}{\bar{L}}, \tag{15a}$$

$$w(x) = \frac{\bar{w}(\bar{x})}{\bar{L}}. \tag{15b}$$

In keeping with the Kirchhoff hypothesis, transverse displacement is a function only of the x-coordinate, and not the z-coordinate. This means that in this model, the transverse displacement varies only in the axial direction, and not the thickness direction.

The height or thickness of each layer is normalized the same way:

$$h_b = \frac{\bar{h}_b}{\bar{L}}, \tag{16a}$$

$$h_p = \frac{\bar{h}_p}{\bar{L}}. \tag{16b}$$

It is noted here, that with this formulation, of concern will be the ratio between these two parameters. To this end, we define the ratio of the thickness of the secondary layer to that of the baseplate as h_0. Hence,

$$h_0 = \frac{h_p}{h_b} = \frac{\bar{h}_p}{\bar{L}} \frac{\bar{L}}{\bar{h}_b} = \frac{\bar{h}_p}{\bar{h}_b}. \tag{16c}$$

The procedure of normalizing the parameters of the secondary and primary layers is extended for all the material properties of both layers. Hence, an important parameter in this study is the ratio of elastic moduli. For plane stress we see the ratio as:

$$E_0 = \frac{\bar{E}_p}{\bar{E}_b}, \tag{17a}$$

where $\bar{E}_p$ is the axial elastic modulus of the secondary layer and $\bar{E}_b$ is the axial elastic modulus of the baseplate. In the case of plane strain, the pertinent ratio is:

$$E_0 = \frac{\bar{E}_p}{\bar{E}_b} \frac{1 - \nu_b^2}{1 - \nu_p^2}. \tag{17b}$$

At this point, the material properties from the previous section must also be non-dimensionalized. These properties are normalized with respect to the dimensional bending stiffness of the baseplate, $\bar{D}_b$, which was given by Eqs. (11a) and (13a). Thus, the bending stiffness of the baseplate and adhered layer are, respectively:

$$D_b = \frac{\bar{D}_b}{\bar{D}_b} = 1, \tag{18a}$$

$$D_p = \frac{\bar{D}_p}{\bar{D}_b} = E_0 h_0^3, \tag{18b}$$

where $\bar{D}_b$ is the dimensional bending stiffness of the baseplate and $\bar{D}_p$ is the dimensional bending stiffness of the secondary layer.

Likewise, the normalized membrane stiffness of the primary and secondary layers are, respectively,

$$C_b = \frac{\bar{C}_b}{\bar{D}_b} = \frac{12}{h_b^2}, \tag{19a}$$

$$C_p = \frac{\bar{C}_p}{\bar{D}_b} = C_b E_0 h_0, \tag{19b}$$

where $\bar{C}_b$ is the dimensional membrane stiffness of the baseplate and $\bar{C}_p$ is the dimensional membrane stiffness of the second layer.

In a similar fashion, forces are normalized with respect to the half-span length, $\bar{L}$, and the dimensional bending stiffness, $\bar{D}_b$, of the baseplate. A general normalized force per unit length, F, is related to its dimensional counterpart, $\bar{F}$, by the relation

$$F = \frac{\bar{F}\bar{L}^2}{\bar{D}_b}. \tag{20}$$

The analysis will consider both transverse and axial electric fields. The axial piezoelectric constant of each layer due to a transverse electric field is normalized with respect to a dimensional reference electric field, $\bar{\mathcal{E}}_{ref}$. Therefore, the normalized axial piezoelectric constant due to a transverse electric field for the baseplate and the secondary layer are, respectively,

$$\eta_{31}^b = \bar{\eta_{31}^b}\bar{\mathcal{E}}_{ref}, \tag{21a}$$

$$\eta_{31}^p = \bar{\eta_{31}^p}\bar{\mathcal{E}}_{ref}. \tag{21b}$$

The ratio of these two properties is defined as

$$\eta_{31}^0 = \frac{\eta_{31}^p}{\eta_{31}^b}. \tag{22}$$

When the electric field is in the transverse direction, it is normalized by the same dimensional reference electric field:

$$\mathcal{E} = \frac{\bar{\mathcal{E}} - \bar{\mathcal{E}}_{ref}}{\bar{\mathcal{E}}_{ref}}. \tag{23}$$

Analogously, if we consider an axial electric field, instead of a transverse one, then the piezoelectric constants that enter the formulation are $\eta_{11}^{\bar{b}}$ and $\eta_{11}^{\bar{p}}$. Both will be normalized with respect to the same dimensional reference electric field. Thus, the normalized counterparts are as follows:

$$\eta_{11}^{b} = \eta_{11}^{\bar{b}} \bar{\mathcal{E}}_{ref}, \tag{24a}$$

$$\eta_{11}^{p} = \eta_{11}^{\bar{p}} \bar{\mathcal{E}}_{ref}. \tag{24b}$$

The ratio of these two properties is defined as

$$\eta_{11}^{0} = \frac{\eta_{11}^{p}}{\eta_{11}^{b}}. \tag{25}$$

The electric field is normalized in the same manner:

$$\mathcal{E} = \frac{\bar{\mathcal{E}} - \bar{\mathcal{E}}_{ref}}{\bar{\mathcal{E}}_{ref}}. \tag{26}$$

2.5 Energy Formulation

The governing equations for each region, and the boundary and matching conditions come about by applying the theorem of stationary potential energy and, hence, as a consequence of taking the first variation of the total potential energy of the system. The potential energy functional of the system is formulated in terms of the strain energies of each layer, as well as a constraint functional for the bonded region. In addition, the internal electrical energy functional is included. The potential energy, Π, of the entire structure is given as follows:

$$\Pi = \sum_{i=1}^{2} \left[U_{B;b}^{(i)} + U_{M;b}^{(i)}\right] + U_{B;p} + U_{M;p} + U_{\mathcal{E}} - \Lambda, \tag{27}$$

where the bending energies of the baseplate and the secondary layer in the two regions are given by

$$U_{B;b}^{(i)} = \int_{S_i} \frac{1}{2} D_b \kappa_b^2 \, dx \quad \text{for } i = 1, 2, \tag{28a}$$

$$U_{B;p} = \int_{S_1} \frac{1}{2} D_p \kappa_p^2 \, dx. \tag{28b}$$

The stretching energies of the baseplate and the secondary layer in the two regions are given by

$$U_{M;b}^{(i)} = \int_{S_i} \frac{1}{2} C_b (e_{bi} - \eta^b \mathcal{E})^2 \, dx \quad \text{for } i = 1, 2, \tag{28c}$$

$$U_{M;p} = \int_{S_1} \frac{1}{2} C_p (e_p - \eta^p \mathcal{E})^2 \, dx. \tag{28d}$$

We consider only the situation where the electric field is prescribed. Consequently, the variation of the internal electrical energy term, $U_{\mathcal{E}}$ will vanish identically, and the details of the form of $U_{\mathcal{E}}$ need not be considered here.

The constraint functional is given by:

$$\Lambda = \int_{S_1} \lambda_1 (w_p - w_b) \, dx + \int_{S_1} \lambda_2 (u_p^* - u_b^*) \, dx, \tag{28e}$$

where λ_1 and λ_2 are Lagrange multipliers which physically correspond to the interfacial normal and shear stresses between the two layers in the bonded region, respectively.

For the problems considered here, there are no applied work terms. It will be seen in what follows that the increase in the electric field will manifest itself through a matching boundary condition as an electro-mechanical moment.

The theorem of stationary potential energy is invoked, which states that for equilibrium solutions the first variation of the potential energy functional must vanish. Hence,

$$\delta\Pi = 0, \tag{29}$$

where δ is the variational operator. This gives rise to the governing equations of equilibrium for each region, as well as the boundary conditions at $x = 0$, $x = 1$, and $x = L_p$ (the boundary between the two regions).

An important point of clarification must be made here. It is well-known that a structure will always tend towards a state of minimum potential energy. Enforcing that the first variation of potential energy vanishes guarantees us only that our solution corresponds to an extremum. It does not guarantee that the corresponding equilibrium configuration is stable. It does not distinguish between a minimum or a maximum of potential energy. Thus, the vanishing of the first variation of the potential energy is necessary to ensure that the configuration will minimize the potential energy of the structure, but it is not a sufficient condition.

We are considering a geometrically nonlinear structure, which means multiple equilibrium configurations are possible for a given value of the loading parameter. Therefore, we must assess the stability of these equilibrium configurations by ensuring that the second variation of the potential energy for these configurations is a positive definite quantity. This, along with the theorem of stationary potential energy is sufficient to determine if a configuration minimizes potential energy (See for example Lanczos [7]).

2.6 Equilibrium Equations

The governing equations for the membrane forces in S_1 and S_2 follow from the variational principle as:

$$\frac{\partial N^*}{\partial x} = 0 \quad \text{in } S_1, \tag{30a}$$

$$\frac{\partial N_b}{\partial x} = 0 \quad \text{in } S_2, \tag{30b}$$

where N^* corresponds to the normalized membrane force in each region. Correspondingly, there is a matching boundary condition at $x = L_p$:

$$N^*(L_p) = N_b(L_p). \tag{31}$$

Though this is a boundary condition, it is worth including in this section because it greatly simplifies the governing equations. Upon combing Eqs. (30a), (30b), and (31) it can be easily seen that the membrane force is uniform throughout the structure. This is stated as

$$N^*(x) = N_b(x) = -N_0 \quad \text{in } S = S_1 + S_2, \tag{32}$$

where the constant N_0 is to be determined as part of the solution.

The governing equations for transverse equilibrium that arise from Eq. (29) take the forms

$$D^* w_1'''' - (N^* w_1')' = 0 \quad \text{in } S_1, \tag{33a}$$

$$D_b w_2'''' - (N_b w_2')' = 0 \quad \text{in } S_2, \tag{33b}$$

where $w_1(x)$ and $w_2(x)$ represent transverse displacement in Region 1 and Region 2, respectively. The above coupled differential equations would render themselves nonlinear, except for the fact that Eq. (32) tells us that the membrane forces are constant, and thus can be pulled outside of the differentiation. Applying Eq. (32) to Eqs. (33a) and (33b) yields:

$$D^* w_1'''' + N_0 w_1'' = 0 \quad \text{in } S_1, \tag{34a}$$

$$D_b w_2'''' + N_0 w_2'' = 0 \quad \text{in } S_2, \tag{34b}$$

which is a solvable linear system of differential equations.

2.7 Constitutive Relations

The potential energy functional was formulated in terms of each layer, individually. In the stacked region, equations for both layers were combined to get the normalized resultant membrane force and normalized bending moment of the composite region, as a whole. They are given in terms of the material properties of the stacked region as follows:

$$N^* = C^* e^* + B^* \kappa^* - n^* \mathcal{E}, \tag{35a}$$

$$M^* = B^* e^* + A^* \kappa^* - r^* \mathcal{E} = D^* \kappa^* + \rho^* N^* - m^* \mathcal{E}, \tag{35b}$$

where $e^*(x)$ is the membrane strain for the stacked region at the reference surface, $\kappa^*(x)$ is the normalized curvature change for the stacked region at the reference surface, and $\mathcal{E}$ corresponds to the normalized uniform electric field change.

The non-dimensional composite material properties are found in terms of the corresponding membrane stiffness, C_b and bending stiffness, D_b of the baseplate, and the membrane and bending stiffnesses of the secondary layer, C_p and D_p. The relations follow as:

$$C^* = C_b + C_p, \tag{36a}$$

$$B^* = \frac{1}{2}(h_p C_p - h_b C_b), \tag{36b}$$

$$A^* = D_b + D_p + \frac{1}{4}C_b h_b^2 + \frac{1}{4}C_p h_p^2, \tag{36c}$$

$$n^* = \eta_{31}^0 C_p + C_b, \tag{36d}$$

$$r^* = \frac{1}{2}\eta_{31}^0 h_p C_p - \frac{1}{2}h_b C_b, \tag{36e}$$

when the applied electric field is in the 3-direction (transverse). When, however, the applied electric field is in the 1-direction (axial), Eqs. (36d) and (36e) become:

$$n^* = \eta_{11}^0 C_p + C_b, \tag{37a}$$

$$r^* = \frac{1}{2}\eta_{11}^0 h_p C_p - \frac{1}{2}h_b C_b, \tag{37b}$$

For mathematical convenience, we also define D^*, m^*, and ρ^* in terms of the previously defined quantities:

$$D^* = A^* - \rho^* B^*, \tag{38a}$$

$$m^* = r^* - \rho^* n^*, \tag{38b}$$

$$\rho^* = \frac{B^*}{C^*}, \tag{38c}$$

where ρ^* physically corresponds to the distance of the centroid of the stacked region with respect to the reference surface.

2.8 Boundary Conditions

In addition to the governing equations that come about from the vanishing of the first variation of the potential energy functional, this formulation also clearly defines the boundary and matching conditions. As previously mentioned, two different boundary conditions are studied: clamped-fixed boundaries and hinged-fixed boundaries. For both of these cases, the fixed constraint means that axial deflections of the structure are prohibited. This is stated, formally, as

$$u^*(0) = 0 \tag{39a}$$

$$u_b(1) = 0 \tag{39b}$$

The remaining boundary conditions for each case are stated explicitly in this section.

2.8.1 Clamped-Fixed Supports

At the fixed end ($x = 1$), the structure cannot displace and is constrained from rotating. Thus,

$$w_2(1) = 0, \tag{40a}$$

$$w_2'(1) = 0. \tag{40b}$$

Since we also consider symmetric deformations, rotation and transverse shear vanish at the center-span ($x = 0$). Thus,

$$w_1^{'}(0) = 0, \tag{40c}$$

$$D^* w_1^{'''}(0) + N_0 w_1^{'}(0) = 0. \tag{40d}$$

At the interface of the two regions, S_1 and S_2, the matching conditions for displacement, rotation, transverse shear, and bending moment are, respectively,

$$w_1(L_p) = w_2(L_p), \tag{40e}$$

$$w_1^{'}(L_p) = w_2^{'}(L_p), \tag{40f}$$

$$D^* w_1^{'''}(L_p) + N_0 w_1^{'}(L_p) = D_b w_2^{'''}(L_p) + N_0 w_2^{'}(L_p), \tag{40g}$$

$$D^* w_1^{''}(L_p) - \rho^* N_0 - m^* \eta^b \mathcal{E} = D_b w_2^{''}(L_p) + \frac{1}{2} h_b N_0. \tag{40h}$$

We rewrite the matching condition for the bending moment, Eq. (40h), in the following way:

$$D^* w_1^{''}(L_p) - D_b w_2^{''}(L_p) = \mathcal{M}_\lambda = m^* \eta^b \mathcal{E} + (\rho^* + \frac{1}{2} h_b) N_0. \tag{41}$$

This shows that the electric field manifests itself as a bending moment at the interface between S_1 and S_2. We call this parameter, $\mathcal{M}_\lambda$, the *transverse loading parameter* and recognize that this is how the electric load enters the problem.

2.8.2 Hinged-Fixed Supports

We consider the situation where the structure is pinned at $x = 1$ and $z = \frac{h_b}{2}$, where the x-coordinate begins at the centerspan of the structure, and the z-coordinate begins at the surface between the two layers, and is positive downward. This is along the neutral axis of Region S_2. At the fixed end ($x = 1$), the structure cannot displace, but can rotate. However, the curvature change must vanish. Thus,

$$w_2(1) = 0, \tag{42a}$$

$$\kappa_2(1) = 0. \tag{42b}$$

The same symmetric deformations as the clamped case are considered. Thus, at the center-span ($x = 0$), rotation and transverse shear vanish:

$$w_1^{'}(0) = 0, \tag{42c}$$

$$D^* w_1^{'''}(0) + N_0 w_1^{'}(0) = 0. \tag{42d}$$

Again, as was the case with the clamped boundaries, the same interior matching boundary conditions exist at the interface of the two regions, S_1 and S_2. Restating these:

$$w_1(L_p) = w_2(L_p), \tag{42e}$$

$$w_1^{'}(L_p) = w_2^{'}(L_p), \tag{42f}$$

$$D^* w_1^{'''}(L_p) + N_0 w_1^{'}(L_p) = D_b w_2^{'''}(L_p) + N_0 w_2^{'}(L_p), \tag{42g}$$

$$D^{*}w_1^{''}(L_p) - D_b w_2^{''}(L_p) = \mathcal{M}_{\lambda} = m^{*}\eta^{b}\mathcal{E} + (\rho^{*} + \frac{1}{2}h_b)N_0. \tag{42h}$$

where we have already rewritten the moment matching condition to identify the transverse loading parameter.

2.9 Integrability Condition

The governing differential equations were derived from the vanishing of the first variation of the potential energy. This resulted in two coupled nonlinear differential equations in terms of the displacements w and u. These equations were greatly simplified into the form shown by Eq. (34a) and Eq. (34b), when Eq. (32) was applied. This means that the nonlinear coupled differential equations in terms of (u, w) were recast into two uncoupled linear differential equations in terms of (N_0, w).

Thus, we need a relationship between the in-plane displacement and the membrane force. This integrability condition acts as a compatibility relation between the axial displacement and the resulting force. This relation is derived by integrating the composite membrane force and solving for the in-plane displacement, resulting in the following:

$$\begin{aligned} u_2(1) - u_1^{*}(0) = &-\Big[\frac{L_p}{C^{*}} + \frac{L_p^{*}}{C_b}\Big]N_0 + \Big[\frac{n^{*}}{C^{*}}L_p + L_p^{*}\Big]\eta^{b}\mathcal{E} \\ &-\Big[\rho^{*} + \frac{1}{2}h_b\Big]w_1^{'}(L_p) - \sum_{i=1}^{2}\int_{S_i}\frac{1}{2}w_i^{'2}\,dx, \end{aligned} \tag{43}$$

where, $L_p^{*} = 1 - L_p$ is the length of S_2.

Since we only consider boundaries that are fixed with respect to axial displacement, we can impose the boundary conditions on in-plane displacement given by Eqs.

(39a) and (39b). This results in the identity

$$-\left[\frac{L_p}{C^*}+\frac{L_p^*}{C_b}\right]N_0+\left[\frac{n^*}{C^*}L_p+L_p^*\right]\eta^b\mathcal{E}-\left[\rho^*+\frac{1}{2}h_b\right]w_1'(L_p)-\sum_{i=1}^{2}\int_{S_i}\frac{1}{2}{w_i'}^2\,dx=0.\quad(44)$$

Therefore, when the governing equations are solved for w, the integrability condition gives us a direct relation between the applied electric field strength, $\mathcal{E}$, and the resulting membrane force, N_0, throughout the structure. Thus, only discrete combinations of N_0 and $\mathcal{E}$ correspond to equilibrium configurations.

3 Analysis

3.1 Analytical Solution

In this section, the governing differential equations previously derived and given by Eqs. (34a) and (34b) (repeated below)

$$D^* w_1^{''''} + N_0 w_1^{''} = 0 \text{ in } S_1, \tag{32a}$$

$$D_b w_2^{''''} + N_0 w_2^{''} = 0 \text{ in } S_2, \tag{32b}$$

are solved analytically for both clamped-fixed and hinged-fixed boundary conditions, which are described in Sections 2.8.1 and 2.8.2, respectively.

Eqs. (34a) and (34b) are readily solvable ordinary differential equations upon recognizing that N_0, while still unknown, is a constant value. Thus, the deflections w_1 and w_2 will be functions of the unknown N_0. The membrane force N_0 can be determined by substituting w_1 and w_2 into the integrability condition, Eq. (44). Thus for a prescribed electric field, we will be able to determine the corresponding membrane force and the transverse deflection of the structure.

3.1.1 Clamped-Fixed Supports

When the structure has clamped-fixed boundary conditions, governing equations. (34a) and (34b) are solved analytically along with the boundary conditions given by Eqs. (40a), (40b), (40c), (40d), (40e), (40f), (40g), (41) to get the transverse displacement field for both regions. This gives

$$w_1(x) = \frac{\mathcal{M}_\lambda}{N_0 \mathcal{H}_c} \left\{ \mathcal{H}_c - \sin(k^* L_p) - \sqrt{\frac{D^*}{D_b}} \sin(k L_p^*) \cos(k^* x) \right\} \text{ in } S_1, \tag{45a}$$

$$w_2(x) = -\frac{\mathcal{M}_\lambda}{N_0 \mathcal{H}_c} \sin(k^* L_p) \left\{1 - \cos[k(1-x)]\right\} \text{ in } S_2, \tag{45b}$$

where

$$\mathcal{H}_c = \sin(k^* L_p) \cos(k L_p^*) + \sqrt{\frac{D^*}{D_b}} \cos(k^* L_p) \sin(k L_p^*), \tag{46}$$

and

$$k^* = \sqrt{\frac{N_0}{D^*}} \tag{47a}$$

$$k = \sqrt{\frac{N_0}{D_b}} \tag{47b}$$

3.1.2 Hinged-Fixed Supports

When, the governing equations (34a) and (34b) are solved subject to hinged-fixed boundary conditions given by Eqs. (42a), (42b), (42c), (42d), (42e), (42f), (42g), (42h), the transverse displacement field is found to be:

$$w_1(x) = \frac{\mathcal{M}_\lambda}{N_0 \mathcal{H}_h} \left\{ \mathcal{H}_h - \sqrt{\frac{D^*}{D_b}} \cos(k L_p^*) \cos(k^* x) \right\} \text{ in } S_1, \tag{48a}$$

$$w_2(x) = -\frac{\mathcal{M}_\lambda}{N_0 \mathcal{H}_h} \sin(k^* L_p) \sin[k(1-x)] \text{ in } S_2, \tag{48b}$$

where

$$\mathcal{H}_h = \sqrt{\frac{D^*}{D_b}} \cos(k^* L_p) \cos(k L_p^*) - \sin(k^* L_p) \sin(k L_p^*), \tag{49}$$

3.2 Consequences of Solution Form

For either boundary condition, we see that the transverse displacement has a similar form. For both cases, the displacement in both regions, S_1 and S_2, is always directly proportional to $\mathcal{M}_\lambda$. We see also that for clamped-fixed supports, the transverse displacement is inversely proportional to $\mathcal{H}_c$, while for hinged-fixed boundaries it is inversely proportional to $\mathcal{H}_h$. Thus, it is apparent that when $\mathcal{H}_\alpha$ for $\alpha = c, h$ approaches zero, the deflections grow without bound. For situations where $\mathcal{H}_\alpha$ is identically zero, the deflection is singular. Since $\mathcal{H}_\alpha$ is only a function of material properties and N_0, we can conclude that there is an appropriate membrane force for both cases that makes the deflection singular.

In fact, it is apparent that there are several values of N_0 that make $\mathcal{H}_\alpha$ vanish. The lowest value of N_0 satisfying

$$\mathcal{H}_\alpha = 0 \tag{50}$$

is designated as the critical membrane force (N_{cr}) and is associated with classic Euler type bifurcation (or more appropriately asymptotic buckling since we are considering a stacked structure with a raised neutral axis), if we were considering the case of controlled edge force loading.

However, instead of controlled edge force loading, we are concerned in this study with electric field strength loading. Since we consider boundary types that are always fixed, electric field strength and membrane force cannot be uncoupled, and are related in a nonlinear manner through the previously described integrability condition given by Eq. (43).

Since our analytical solutions given by Eqs. (45a), (45b) and (48a), (48b) show that the transverse displacement is proportional to $\mathcal{M}_\lambda$ for both situations, an appropriate ratio of electric field strength and axial membrane force can be implemented so that $\mathcal{M}_\lambda$ vanishes. For the case when $N_0 = N_{cr}$, $\mathcal{M}_\lambda$ will vanish when

$$\mathcal{E} = \frac{(\rho^* + \frac{h_b}{2})N_{cr}}{\eta^b m^*} \tag{51}$$

When this is the case, we say $\mathcal{E} = \mathcal{E}_{cr}$. It will be shown later that $\mathcal{E}_{cr}$ is a driving factor in the orientation of the structural response of the system.

3.3 Stability Criterion

The geometrically nonlinear nature of the problem lends itself to multiple equilibrium states for given loading conditions. This is apparent by the transcendental and nonlinear nature of the integrability condition, Eq. (43). For a given electric field, it is possible that multiple equilibrium configurations can be obtained. Taking the first variation of the potential energy functional ensured that equilibrium configurations arose when the potential energy functional was stationary. However, these stationary values can represent a minimum or a maximum of potential energy. The propensity of structures to tend towards configurations of minimum potential energy leads to the well accepted conclusion that maximum values of the total potential energy functional correspond to unstable equilibrium configurations, while stable equilibrum configurations are associated with a minimum value of potential energy. Thus, it is important to have a criterion for deciding to which equilibrium configuration the structure will tend.

Since this is a quasi-static solution, it is important to clarify at this point what is meant by stability. An equilibrium configuration is considered stable if, when perturbed away from a state of equilibrium, it will tend back to the same equilibrium state. Any other result is deemed unstable.

Stability of our solution depends upon the second variation of the potential energy functional. In fact the solution is deemed stable when

$$\delta^2\Pi > 0. \tag{52}$$

The system is perturbed away from its equilibrium states by perturbing the transverse displacement, w, and the axial displacement, u. It was shown earlier by Eqs. (45a), (45b), (48a) and (48b) that w is always directly proportional to the transverse loading parameter, $\mathcal{M}_\lambda$, given by Eq. (41). Thus, perturbing $\mathcal{M}_\lambda$ is equivalent to perturbing w.

We also know that the axial strain, e, depends directly upon u. So we can perturb e, instead of u. Moreover, perturbing e is equivalent to perturbing the membrane force N_0. Consequently, we write the second variation of the total potential energy, in terms of $\delta\mathcal{M}_\lambda$ and δN_0, which is equivalent to perturbing w and u. The second variation of the total potential energy takes the following form,

$$\begin{aligned}\delta^2\Pi = \frac{1}{4N_0\mathcal{H}_c^2}\Big[\frac{D^*}{D_b}k^*\sin^2(kL_p^*)\sin(2k^*L_p) + k\sin^2(k^*L_p)\sin(2kL_p^*)\Big](\delta\mathcal{M}_\lambda)^2 \\ +\frac{1}{2}\Big[\frac{L_p}{C^*}+\frac{L_p^*}{C_b}\Big](\delta N_0)^2,\end{aligned} \tag{53a}$$

$$\begin{aligned}\delta^2\Pi = \frac{1}{4N_0\mathcal{H}_h^2}\Big[\frac{D^*}{D_b}k^*\cos^2(kL_p^*)\sin(2k^*L_p) - k\sin^2(k^*L_p)\sin(2kL_p^*)\Big](\delta\mathcal{M}_\lambda)^2 \\ +\frac{1}{2}\Big[\frac{L_p}{C^*}+\frac{L_p^*}{C_b}\Big](\delta N_0)^2,\end{aligned} \tag{53b}$$

for clamped and hinged boundaries, respectively.

As stated by Eq. (52), stability of an equilibrium configuration requires that the second variation of the total potential energy is positive definite. To check this, Eqs. (53a) and (53b) are rewritten in canonical form as

$$\begin{bmatrix} \frac{\mathcal{F}}{N_0} & 0 \\ 0 & \zeta \end{bmatrix} \begin{bmatrix} (\delta\mathcal{M}_\lambda)^2 \\ (\delta N_0)^2 \end{bmatrix} > 0, \tag{54}$$

where

$$\zeta = \frac{1}{2}\Big[\frac{L_p}{C^*} + \frac{L_p^*}{C_b}\Big], \tag{55}$$

and

$$\mathcal{F} = \frac{1}{4\mathcal{H}_c^2}\Big[\frac{D^*}{D_b}k^* \sin^2(kL_p^*)\sin(2k^*L_p) + k\sin^2(k^*L_p)\sin(2kL_p^*)\Big], \tag{56a}$$

$$\mathcal{F} = \frac{1}{4\mathcal{H}_h^2}\Big[\frac{D^*}{D_b}k^* \cos^2(kL_p^*)\sin(2k^*L_p) - k\sin^2(k^*L_p)\sin(2kL_p^*)\Big]. \tag{56b}$$

for clamped and hinged boundaries, respectively.

Clearly, $(\delta\mathcal{M}_\lambda)^2$ and $(\delta N_0)^2$ are positive definite since each represents a physical quantity squared. Thus, we need to only consider positive definiteness of the characteristic matrix in Eq. (54). This is a symmetric matrix, which is positive definite when it's eigenvalues are both positive definite. Since the characteristic matrix is already diagonal, the eigenvalues are clearly:

$$\lambda_1 = \frac{\mathcal{F}}{N_0}, \tag{57a}$$

$$\lambda_2 = \zeta. \tag{57b}$$

It is apparent that, since L_p, L_p^*, C_b, and C^* are all positive values (as defined earlier),

$$\zeta > 0, \tag{58}$$

always. The configuration is now considered stable if $\lambda_1 > 0$. This would imply that $\mathcal{F} > 0$. Therefore, we call $\mathcal{F}$ the stability function. An equilibrium configuration is stable if and only if

$$\mathcal{F} > 0, \tag{59}$$

where $\mathcal{F}$ is given by Eq. (56a) or Eq. (56b) depending on whether the supports are clamped or hinged, respectively.

Now that the governing equations have been solved and a measure of stability has been assessed, we can know which equilibrium path the structure will tend towards. Results of numerical simulations for many different cases are shown in the next chapter. The stability analysis helps to draw definitive conclusions about the buckling and post-buckling nature of these structures.

4 Results and Discussion

This chapter presents results of numerical simulations for the layered structures discussed earlier, which are restricted from in-plane motion. The loading scenario considered here is a uniform increase in electric field strength. As stated earlier, the two different boundary conditions to be studied are clamped and hinged, respectively.

Solution of the governing equations with the aid of the stability analysis, implementation of the boundary and matching conditions, in addition to utilization of the integrability condition, gives rise to various load-deflection paths for our structure. Several different material combinations are presented to demonstrate the qualitative behavior of sling-shot buckling. These results show how and when sling-shot buckling will occur.

Critical parameters will be identified, and a complete parameter study is given to show the buckling behavior of the structure under different geometries, as well as material properties. This section gives insight to the role these parameters play in facilitating this unique buckling phenomenon.

4.1 Representative Results

4.1.1 Clamped-Fixed Supports

It is instructive to first discuss a stacked structure whose two layers have the same mechanical material properties, but with differing piezoelectric constants. This is done so that we can isolate the difference between the piezoelectric effect in the two layers, and study more closely the role it plays in the overall behavior of the structure.

We are focusing here on how the piezoelectric effect influences sling-shot buckling. We will assume, for our first numerical analysis, that the structure is subjected to a transverse electric field, and that it has clamped-fixed boundary conditions. The structure to be analyzed has the following properties:

$$h_b = h_p = 0.06,$$

$$L_p = 0.75,$$

$$E_0 = 1.0,$$

$$\eta_{31}^b = 0.003.$$

$$\eta_{31}^0 = 0.5.$$

The results for this situation are also valid when considering a structure where the electric field is applied in an axial manner, with the structure having piezoelectric properties $\eta_{11}^b = 0.003$ and $\eta_{11}^p = 0.0015$.

Based on these values, we can calculate the critical non-dimensional membrane force, N_{cr}, and critical non-dimensional electric field strength, $\mathcal{E}_{cr}$. Substitution of Eq. (46) into Eq. (50) results in $N_{cr} = 36.16$. Upon substituting this value into (51), it is found that $\mathcal{E}_{cr} = 7.233$.

As mentioned in Section 2.9, the integrability condition gives discrete combinations of N_0 and $\mathcal{E}$ that correspond to equilibrium configurations. Due to the geometrically non-linear strain-displacement formulation, the correspondence is not one-to-one. For the properties chosen above, the electric field strength is varied, and the corresponding membrane forces are calculated by numerically solving Eq. (44) for N_0. The results are shown in Figure 8.

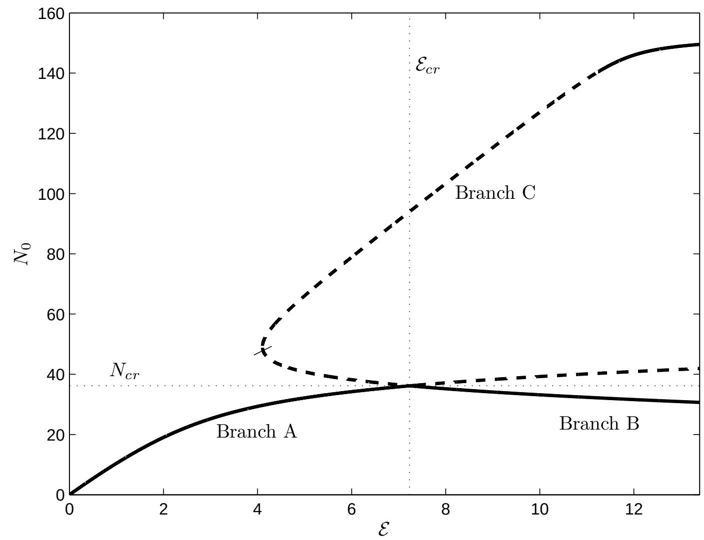

Figure 8: Clamped-fixed boundaries: Equilibrium pairs of applied electric field, $\mathcal{E}$, and corresponding reactionary membrane force, N_0.

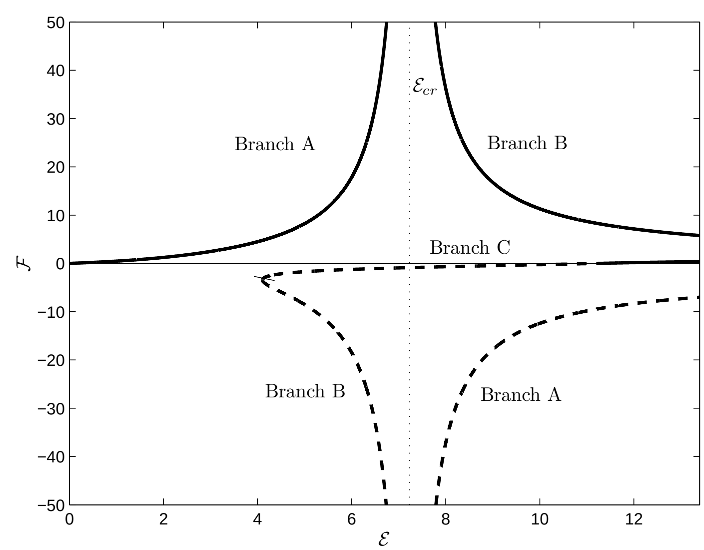

Figure 9: Clamped-fixed boundaries: Stability criterion, $\mathcal{F}$, as a function of the applied electric field, $\mathcal{E}$.

It is apparent from Figure 8 that for small electric fields, the membrane force can only be single-valued. However, when the non-dimensional electric field exceeds 4.10, there exists three possible values of N_0 that correspond to equilibrium solutions, as shown on the figure. The equilibrium curves are labeled branches A, B, and C, respectively, in order to keep track of them in Figures 9 - 11.

To decide what the actual membrane force will be, it is instructive to check the stability of the three membrane forces. The criterion for stability, derived in Section 3.3, shows that the structure is in a stable equilibrium configuration when $\mathcal{F}$, the so called stability function (given by Eq. (56a)), is positive. The equilibrium pairs of $(\mathcal{E},\, N_0)$ depicted in Figure 8 are substituted into the stability function, and shown graphically in Figure 9. Stable pairs are shown as solid curves, while the unstable equilibrium configurations are shown by dashed curves. The stability results are added to the other corresponding figures for clarity, meaning that in all figures a solid curve represents a stable configuration, whereas a dashed curve represents an unstable configuration.

Thus, we see from Figure 8 that the true value of N_0 is that of branch A, up until the critical electric field is reached. At this point, branch B is the only stable configuration. As the electric field increases, branch B is the only one corresponding to a stable solution. However, when the non-dimensional electric field strength reaches 11.24, in this situation, branch C also has stable equilibrium configurations. The natural question to ask at this point is, how can one decide which stable equilibrium configuration the structure will tend towards?

Figure 10 shows the total potential energy of the structure as a function of the applied electric field strength. This is computed by substituting the equilibrium pairs of ($\mathcal{E}$, N_0) into the total potential energy functional given by Eq. (27). It is well known that a structure will tend towards the state of lowest potential energy. It is seen that when the electric field reaches $\mathcal{E}_{cr}$, branch B corresponds to a lower energy state than branch A, which is why the structure switches from A to B at this point. It is also seen that when the electric field strength gets to 11.24, both branches B and C are stable. However, branch B is much more energetically favorable than branch C, so the structure will continue along following the equilibrium path of branch B.

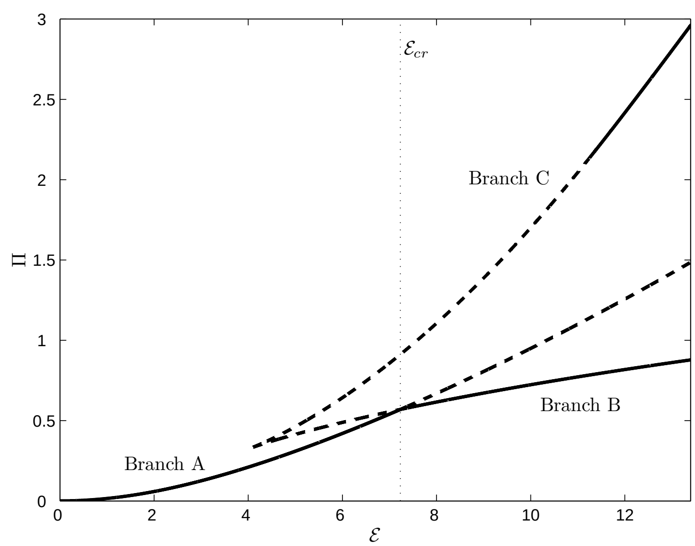

Figure 10: Clamped-fixed boundaries: Potential energy, Π, of the structure as a function of the applied electric field, $\mathcal{E}$.

At this point, for a uniformly increasing electric field, we are able to tell exactly what the value of the membrane force, N_0, is for any electric field. These values are substituted into the equations for transverse deflection, given by (45a) and (45b). The centerspan deflection (i.e. $w_1(0)$) is plotted as a function of the applied electric field in Figure 11. Once again, the stability results are added to this load-deflection graph. It can be seen that as the electric field increases from zero, the structure will deflect in the upwards sense. However, once the critical electric field is reached, branch A becomes unstable, and the structure will tend towards branch B. Branch B, as shown by the figure, is associated with downward deflections. Thus, at this point where the critical membrane force and critical electric field are reached simultaneously, the structure dynamically shifts from upward to downward deflections. Therefore, the structure exhibits sling-shot buckling at this point. An increase in electric field strength means the structure will continue to deflect downward following the path of branch B. Again, it is worth noting that branch C eventually becomes stable, but the energy argument makes that equilibrium configuration impossible to attain naturally. The magnitude of the deflections shown in Figure 11 show that the sling-shot buckling instability occurs well within the allowable deflection bounds of beam theory, validating the appropriateness of the model.

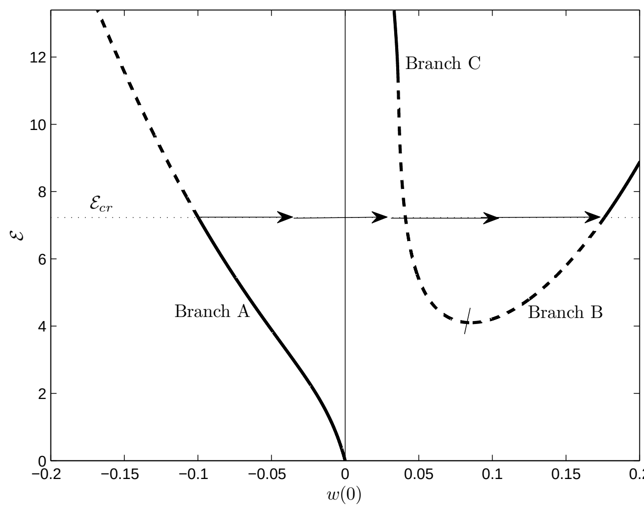

Figure 11: Clamped-fixed boundaries: Load-deflection curve: centerspan displacement, $w(0)$, as a function of the applied electric field, $\mathcal{E}$.

4.1.2 Hinged-Fixed Supports

Figures 12, 13, 14, and 15 show results for the same geometric and material properties as before, but with hinged-fixed, as opposed to clamped-fixed boundary conditions. We see the same qualitative behavior in the hinged case that was observed in the clamped case. Three branches of equilibrium configuration exist, just as before. It is important to notice that for the hinged case, $N_{cr} = 16.11$ and $\mathcal{E}_{cr} = 3.222$. These values are significantly less than those for the clamped case. A beam or plate that is fixed only at one point of contact on its edges is physically much more susceptible to transverse deflection than one that is fixed at every point on its boundary. Thus, the hinged structure requires a much smaller electric field to induce transverse deflections. Therefore, it makes sense for the critical membrane force and critical electric field to be lower than those for the clamped case.

It is also worth noting from comparing Figure 15 with Figure 11, that the magnitude of the critical deflection is smaller for the hinged case. That is, sling-shot buckling occurs not only at a lower electric field and corresponding membrane force, but also when the structure has deflected less than the clamped case.

Comparison of Figures 14 and 10 shows that, for a given electric field, the hinged structure always has less stored potential energy than the clamped structure. This makes perfect physical sense based on the constraints on the boundaries. A clamped structure, inherently, leads to a more constrained displacement field than one that is hinged. Thus, when the structure does deflect, the clamped one is less flexible and therefore stores more energy than the hinged configuration.

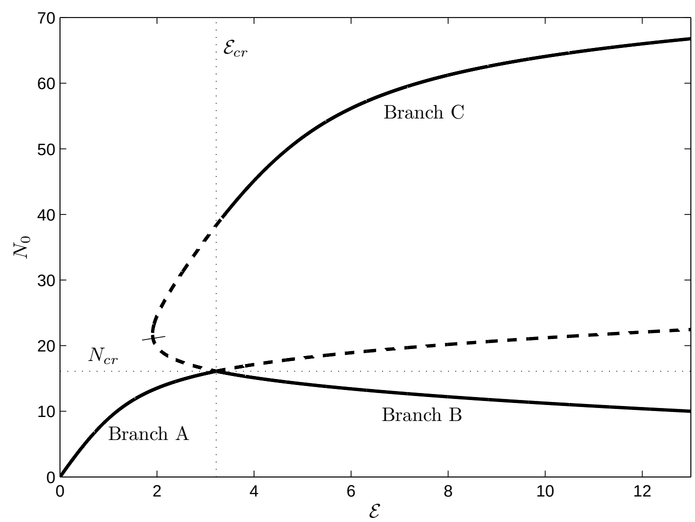

Figure 12: Hinged-fixed boundaries: Equilibrium pairs of applied electric field, $\mathcal{E}$, and corresponding reactionary membrane force, N_0.

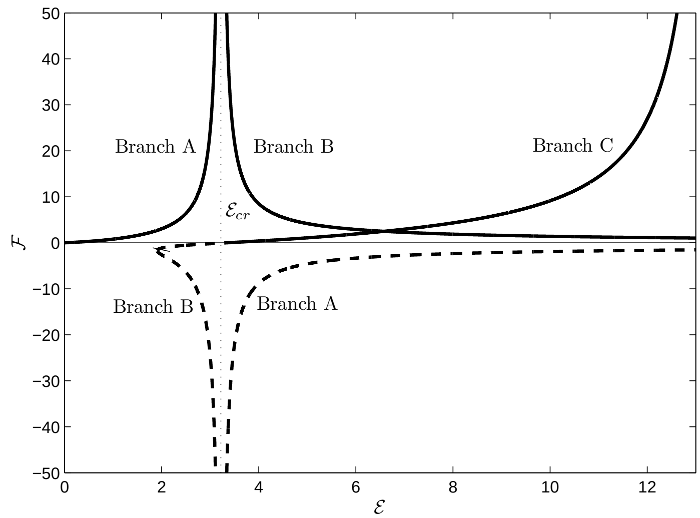

Figure 13: Hinged-fixed boundaries: Stability criterion, $\mathcal{F}$, as a function of the applied electric field, $\mathcal{E}$.

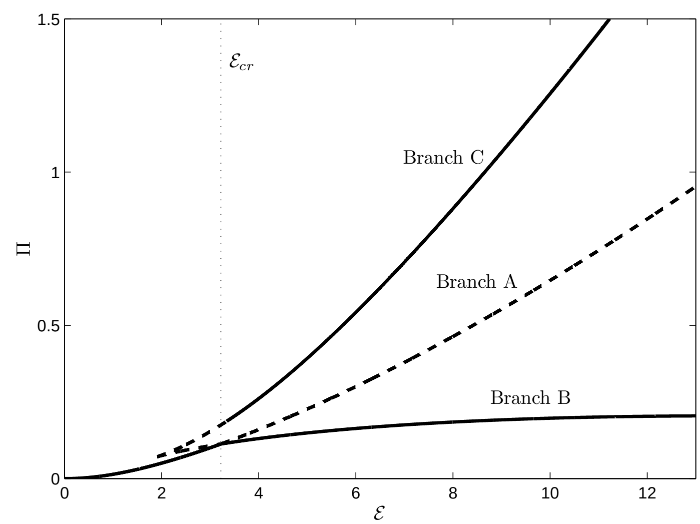

Figure 14: Hinged-fixed boundaries: Potential energy, Π, of the structure as a function of the applied electric field, $\mathcal{E}$.

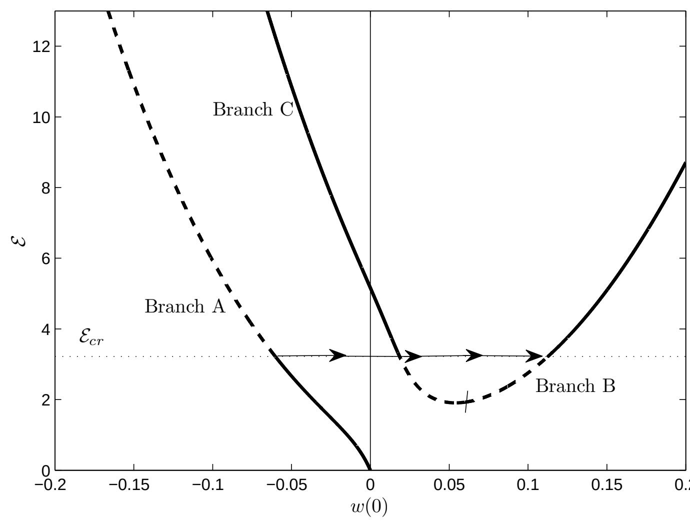

Figure 15: Hinged-fixed boundaries: Load-deflection curve: centerspan displacement, $w(0)$, as a function of applied electric field, $\mathcal{E}$.

A point of clarification needs to be made regarding the stability of the hinged-fixed case. While it appears in Figure 13 that branch C becomes unstable at the critical electric field, this is in fact untrue. Figure 16 shows a magnified view of Figure 13. From this, it is apparent that branch C switches from an unstable to a stable curve at $\mathcal{E} = 3.341$, not at $\mathcal{E} = \mathcal{E}_{cr} = 3.222$. Coupling this information with the energy argument we made for the clamped case, it is clear that at the critical electric field, the structure will switch from branch A to branch B, while branch C is still physically unrealizable.

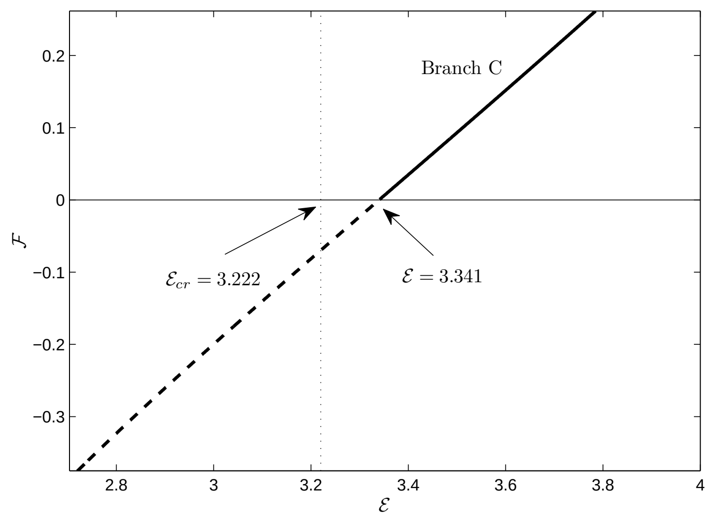

Figure 16: Hinged-fixed boundaries: Closer view of the difference between the critical electric field and the point where branch C switches from an unstable to a stable configuration.

4.2 Critical Parameter Study

The previous section showed that sling-shot buckling is possible in piezoelectric structures. For temperature controlled loading of non-piezoelectric materials, Karlsson and Bottega (2000) [4] proved that sling-shot buckling only occurs for structures where $0 < \alpha_0 < 1$, where α_0 is the ratio of the non-dimensional coefficient of thermal expansion of the secondary layer to that of the primary layer. This is a question that needs to be addressed for the piezoelectric situation.

Figures 17 - 20 are the graphs for the same clamped-fixed structure as the previous section, but with different ratios of piezoelectric constants. They represent the case where the two materials have the same piezoelectric constant, $\eta_{31}^p = \eta_{31}^b = 0.003$ or $\eta_{11}^p = \eta_{11}^b = 0.003$, depending on whether the structure is subjected to a transverse or axial electric field. Thus, $\eta^0 = 1$. Figure 17 shows the discrete combinations of applied electric field and resultant axial membrane force, as given by the integrability condition. We see for this case that branch A and branch B asymptote towards each other, but never cross. The critical membrane force for this case is the same as before ($N_{cr} = 36.16$), as the piezoelectric constants do not affect this. Recall, the critical electric field is calculated by Eq. (51) (repeated below):

$$\mathcal{E} = \frac{(\rho^* + \frac{h_b}{2})N_{cr}}{m^*}. \tag{49}$$

For the case where $\eta^0 = 1$, $m^* = 0$. Thus, there is no critical electric field for this case, and hence sling-shot buckling will not occur.

Figure 18 shows the stability of the three equilibrium branches. It is apparent that branch A is always stable, while branch B is never stable, and branch C transitions from unstable to stable. Based on Figure 19 it is apparent that the potential energy of the stable region of branch C is far greater than that of branch A. Thus, the structure will continue along branch A as the electric field increases. Finally, the load-deflection profile is given by Figure 20. It shows that as the electric field increases, the structure will continually deflect upwards in the context of this model. Therefore, sling-shot buckling will not occur when then piezoelectric constants of the two layers are equal. Sling-shot buckling is precipitated by a mismatch in piezoelectric constants, which is not the case here.

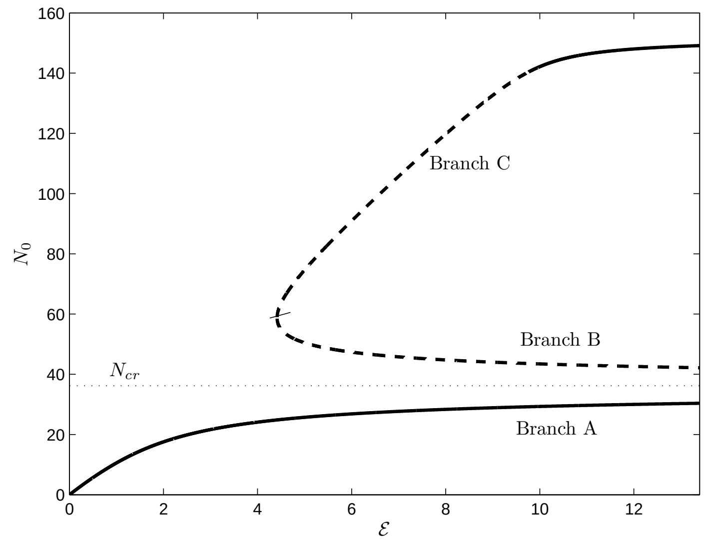

Figure 17: Clamped-fixed boundaries, $\eta^0 = 1$: Equilibrium pairs of applied electric field, $\mathcal{E}$, and corresponding reactionary membrane force, N_0.

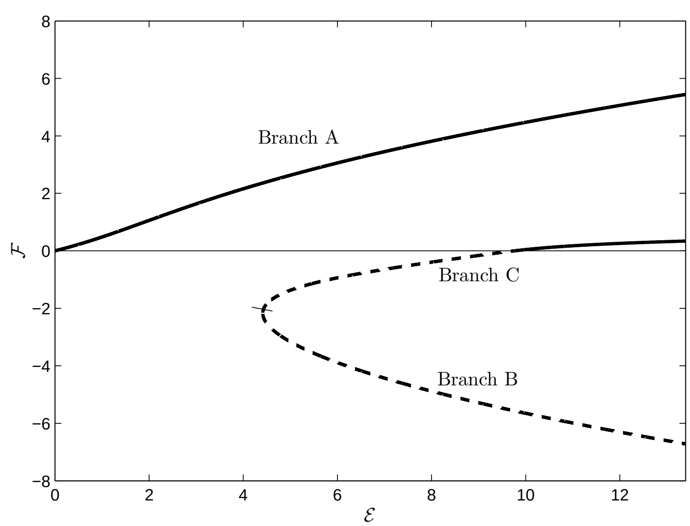

Figure 18: Clamped-fixed boundaries, $\eta^0 = 1$: Stability criterion, $\mathcal{F}$, as a function of the applied electric field, $\mathcal{E}$.

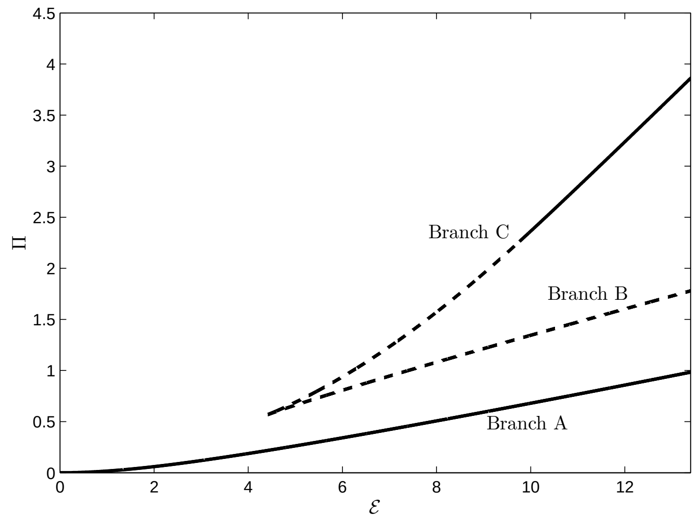

Figure 19: Clamped-fixed boundaries, $\eta^0 = 1$: Potential energy, Π, of the structure as a function of the applied electric field, $\mathcal{E}$.

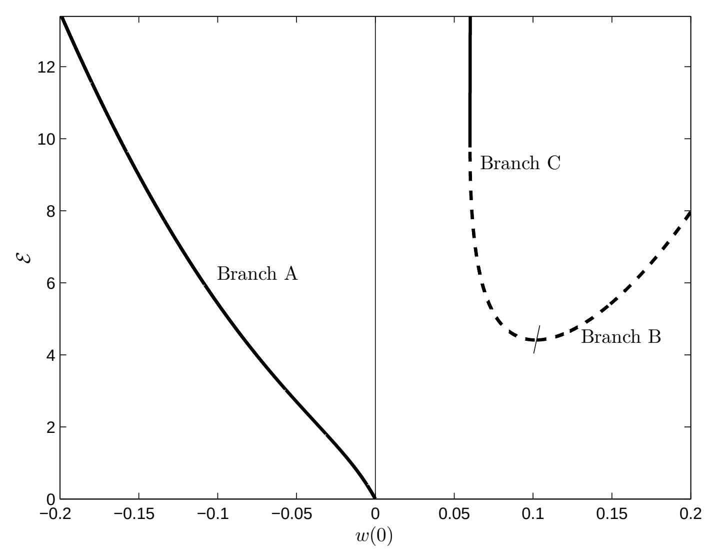

Figure 20: Clamped-fixed boundaries, $\eta^0 = 1$: Load-deflection curve: centerspan displacement, $w(0)$, as a function of applied electric field, $\mathcal{E}$.

One more situation needs to be addressed. Since sling-shot buckling requires a mismatch in piezoelectric constants, will it still occur when the piezoelectric constant of the secondary layer is greater than that of the primary layer? Results for this situation are shown in Figures 21 - 24. Again, we keep the same geometric properties as the previous section, but here $\eta^b_{31} = 0.003$ and $\eta^p_{31} = 0.006$, or $\eta^b_{11} = 0.003$ and $\eta^p_{11} = 0.006$, depending on whether the structure is subjected to a transverse or axial electric field. Thus, $\eta^0 = 2$ for this situation.

When $\eta^0 > 1$, $m^* < 0$. Thus, the critical electric field is mathematically a negative number, which does not correspond to a real physical situation. Therefore, we can say there is no critical electric field for this situation, as well. Figure 21, much like Figure 17, shows that branches A and B never cross each other. Upon inspection of Figure 22, it is apparent that branch B is always unstable, while branch C becomes stable at higher electric fields. Like the previous situation, Figure 23 shows that branch C will never be naturally attained, as it corresponds to much higher potential energy in the system than branch A. Figure 24 shows the load-deflection graph for this situation. As the applied electric field increases, the structure will follow the equilibrium path of branch A. Since there is no critical electric field, an increase in applied electric field will not result in sling-shot buckling.

Based on the mathematical arguments set forth, and aided by the corresponding figures, it can be definitively concluded that sling-shot buckling will only occur when the piezoelectric constant of the baseplate is greater than that of the secondary layer ($0 < \eta^0 < 1$).

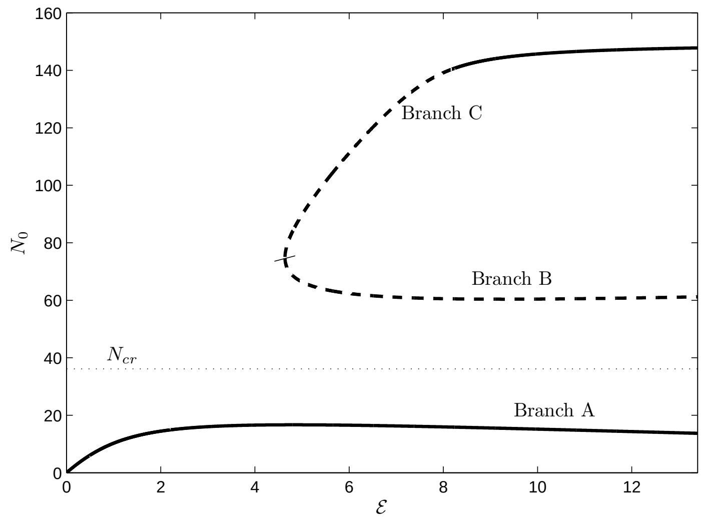

Figure 21: Clamped-fixed boundaries, $\eta^0 = 2$: Equilibrium pairs of applied electric field, $\mathcal{E}$, and corresponding reactionary membrane force, N_0.

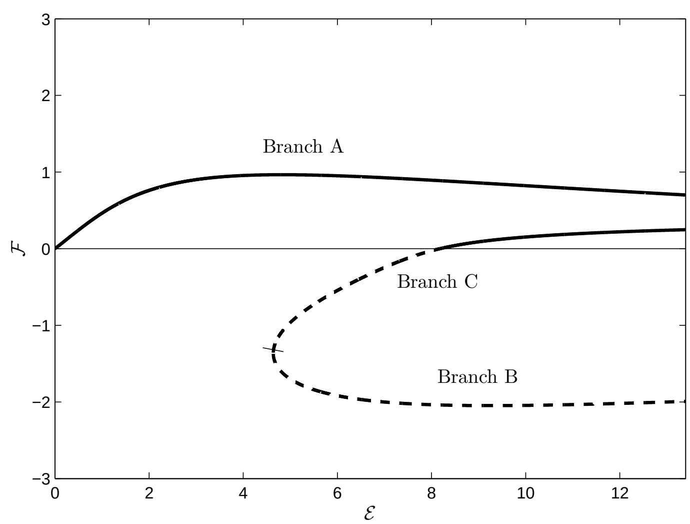

Figure 22: Clamped-fixed boundaries, $\eta^0 = 2$: Stability criterion, $\mathcal{F}$, as a function of the applied electric field, $\mathcal{E}$.

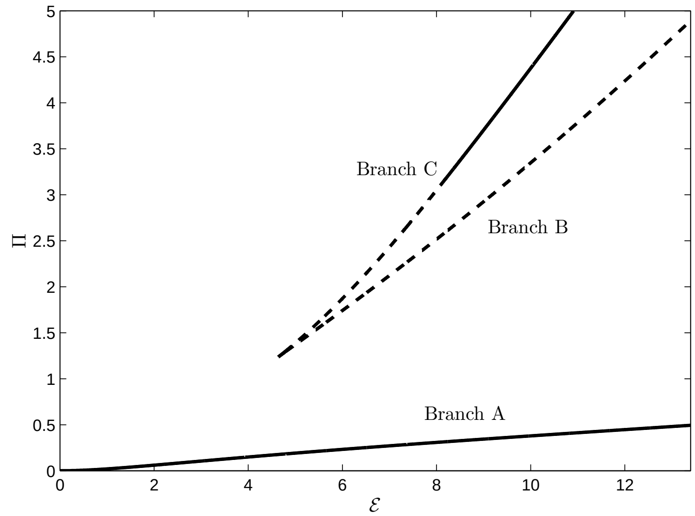

Figure 23: Clamped-fixed boundaries, $\eta^0 = 2$: Potential energy, Π, of the structure as a function of the applied electric field, $\mathcal{E}$.

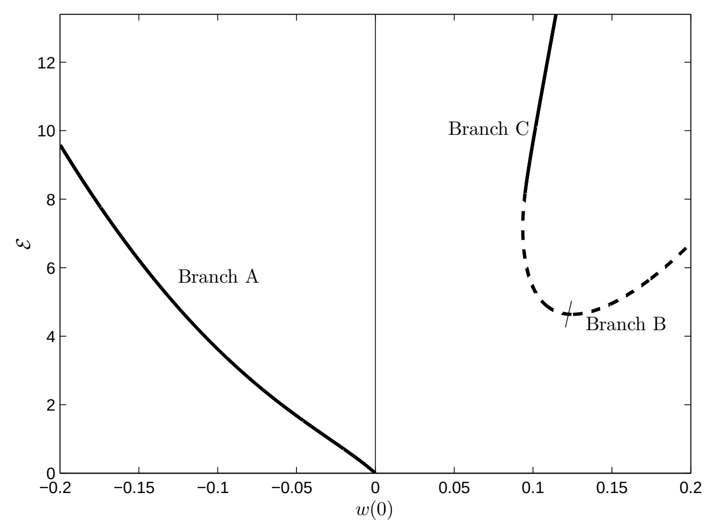

Figure 24: Clamped-fixed boundaries, $\eta^0 = 2$: Load-deflection curve: centerspan displacement, $w(0)$, as a function of applied electric field, $\mathcal{E}$.

4.2.1 Effect of Changing Young's Modulus

Since it is now known that sling-shot buckling will occur when $0 < \eta^0 < 1$, we wish to show how the critical electric field is affected by the other material or geometric properties. The first one to consider is the ratio of the elastic modulus of the secondary layer to that of the primary layer. Figures 25 and 26 show the critical electric field as a function of the ratio of piezoelectric constants for various ratios of elastic moduli, for clamped and hinged boundary conditions respectively. For both of these cases, we assume the same material properties as before: $h_b = h_p = 0.06$, $L_p = 0.75$, and $\eta_{31}^b = 0.003$ (or $\eta_{11}^b = 0.003$). As the secondary layer becomes stiffer, the critical electric field increases. A stiffer secondary layer naturally becomes less susceptible to transverse deflections, and thus will require a higher electric field to buckle. Also, the critical electric field is directly proportional to η^0—a very intuitive result both physically and mathematically speaking. It can also be seen from a comparison of Figure 25 and Figure 26 that the critical electric field for the hinged case is significantly lower than the clamped case, as previously discussed.

Here, we evaluate a combination of actual materials, namely polarized ceramics. Consider a clamped beam (plane stress) with an applied electric field oriented in the axial direction. The primary layer is composed of PZT-5A ($\bar{c}_{11} = 11.1 \times 10^{10}\ N/m^2$, $\bar{\eta}_{11} = 1.423 \times 10^{-10}\ C/N$), while the secondary layer is PZT-7A ($\bar{c}_{11} = 13.1 \times 10^{10}\ N/m^2$, $\bar{\eta}_{11} = 7.252 \times 10^{-11}\ C/N$). The pertinent ratios here are $E_0 = 1.180$ and $\eta_{11}^0 = 0.510$. This configuration is shown in Figure 25.

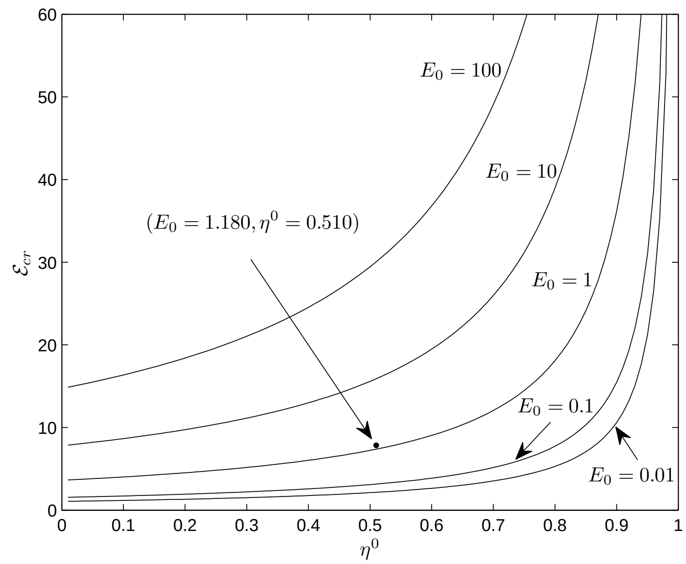

Figure 25: Clamped-fixed boundaries: Critical electric field, $\mathcal{E}_{cr}$, as a function of ratio of piezoelectric constants, η^0, for various ratios of Young's Modulus, E_0.

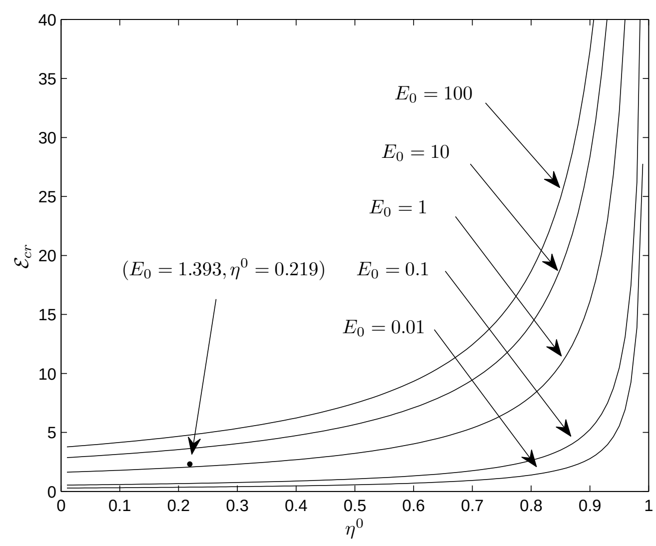

Figure 26: Hinged-fixed boundaries: Critical electric field, $\mathcal{E}_{cr}$, as a function of ratio of piezoelectric constants, η^0, for various ratios of Young's Modulus, E_0.

Likewise, consider a hinged-fixed structure subjected to a state of plane stress, where the primary layer is PZT-5H ($\bar{c}_{11} = 11.7\times10^{10}\ N/m^2$, $\bar{\eta}_{11} = 1.991\times10^{-10}\ C/N$) and the secondary layer is PZT-6B ($\bar{c}_{11} = 16.3\times10^{10}\ N/m^2$, $\bar{\eta}_{11} = 4.356\times10^{-11}\ C/N$). The pertinent ratios here are $E_0 = 1.393$ and $\eta_{11}^0 = 0.219$. This configuration is shown in Figure 26.

4.2.2 Effect of Changing Length of Secondary Layer

The critical electric field, $\mathcal{E}_{cr}$, is also affected by the size of the secondary layer. It is reached when the transverse loading parameter, $\mathcal{M}_\lambda$, vanishes. Eq. (41) shows that the transverse loading parameter represents a competition of moments at the interface between the bonded region and the region with just the primary layer. Clearly this value will be affected by adjusting the length of the bonded region. Figures 27 and 28 show for clamped and hinged boundaries, respectively, that as the bonded region increases the critical electric field is raised—in agreement with the mathematical argument just put forth. For this situation, $h_b = h_p = 0.06$, $E_0 = 1.0$, and $\eta_{31}^b = 0.003$ (or $\eta_{11}^b = 0.003$). Physically, too, we can imagine that as the bonded region increases, the structure is stiffer and thus will require a stronger electric field to deflect, and eventually buckle.

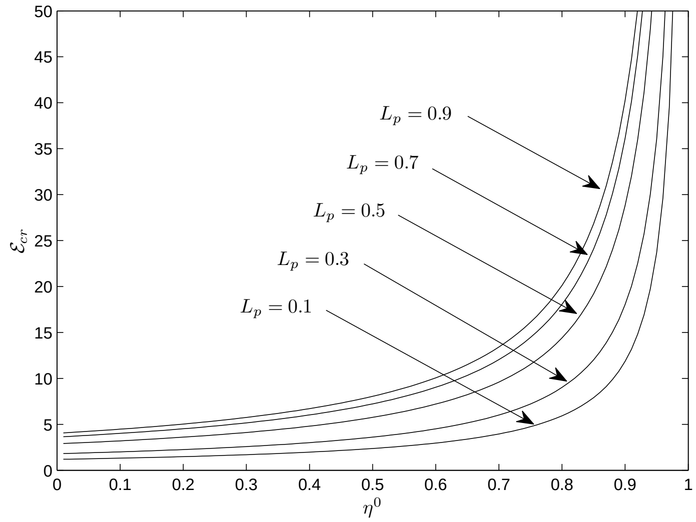

Figure 27: Clamped-fixed boundaries: Critical electric field, $\mathcal{E}_{cr}$, as a function of ratio of piezoelectric constants, η^0, for various values of L_p.

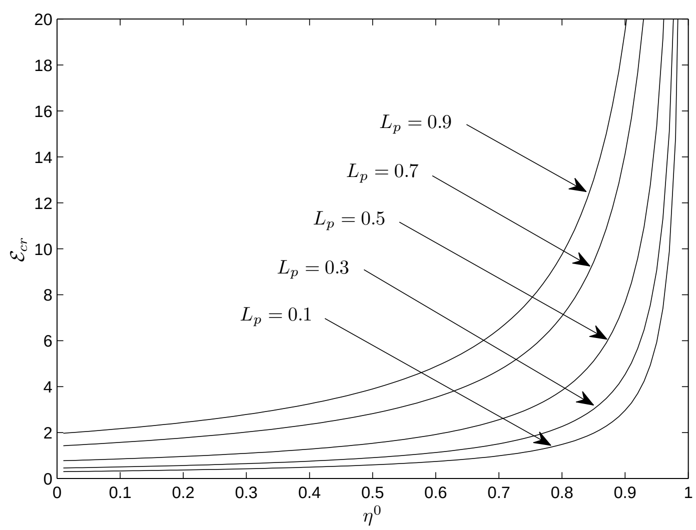

Figure 28: Hinged-fixed boundaries: Critical electric field, $\mathcal{E}_{cr}$, as a function of ratio of piezoelectric constants, η^0, for various values of L_p.

4.2.3 Effect of Changing Thickness Ratio

The final geometric ratio to consider is that of the thickness of the two layers. We see from Figures 29 and 30 that as the secondary layer gets thicker the critical electric field is raised. The parameters chosen for this simulation are as follows: $E_0 = 1$, $h_b = 0.06$, $L_p = 0.75$, and $\eta_{31}^b = 0.003$ (or $\eta_{11}^b = 0.003$). We again see higher critical electric field values for the clamped supports when compared to the hinged supports.

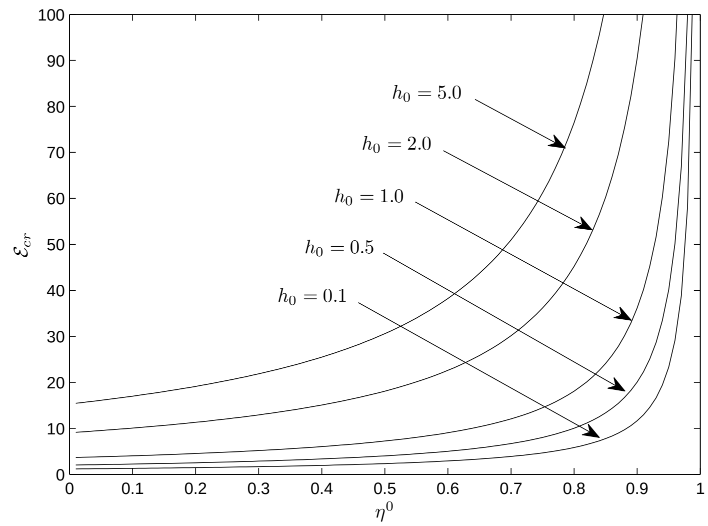

Figure 29: Clamped-fixed boundaries: Critical electric field, $\mathcal{E}_{cr}$, as a function of ratio of piezoelectric constants, η^0, for various thickness ratios, h_0.

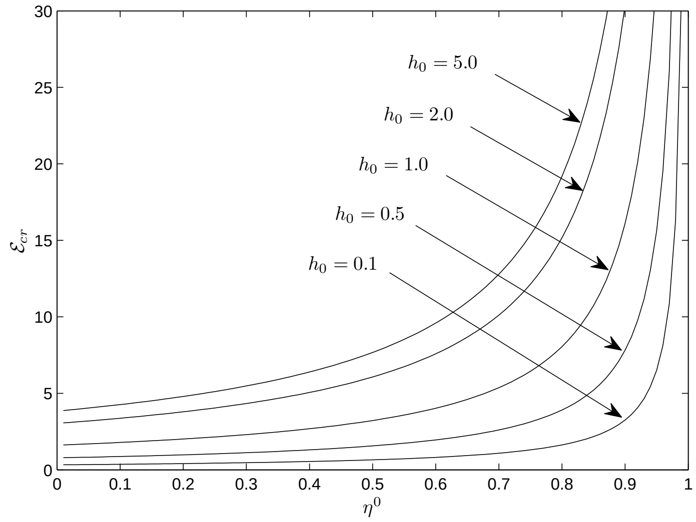

Figure 30: Hinged-fixed boundaries: Critical electric field, $\mathcal{E}_{cr}$, as a function of ratio of piezoelectric constants, η^0, for various thickness ratios, h_0.

5 Conclusion and Future Work

The buckling and post-buckling behavior of layered piezoelectric beam-plates subjected to an externally applied electric field has been studied. The geometrically non-linear problem was self-consistently formulated in the calculus of variations and solved analytically. It was shown that when the structure is constrained from axial deformation, the applied electric field corresponds to discrete combinations of the reactionary membrane force via the integrability condition, which ensures compatibility of the displacement field. Thus, there exists multiple possible deflection paths. By taking the second variation of the total potential energy of the system, stability of the multiple deflection paths is assessed. Finally, the true path the structure will follow is based on the potential energy. Numerical simulations are presented as an example with which to apply these results.

In order to solve the non-linear partial differential equation governing the structure in terms of the transverse and axial displacements, u and w, respectively, the problem was recast into a mixed formulation in terms of N_0 and w. Realizing that the axial membrane force, N_0 was always uniform allowed the non-linear partial differential equation to be transformed into an ordinary differential equation for the transverse deflection, w.

The transverse loading parameter, which comes about as a matching boundary condition ensuring matching moments at the interface of the two regions, has been identified and its importance realized. Because it is directly proportional to the transverse motion of the structure and represents a competition between mechanical and piezoelectric moments at the interface of the two domains, the transverse loading parameter dictates the direction of transverse deflection for a given electric field.

Two major critical parameters were identified: the critical membrane force, N_{cr} and the critical electric field $\mathcal{E}_{cr}$. It was shown that the simultaneous vanishing of these two parameters corresponds to sling-shot buckling. It was argued mathematically and verified by numerical simulations that these parameters can only simultaneously vanish when $0 < \eta^0 < 1$. A parameter study was then presented to show how these values are affected by various geometric and material properties. It was shown that the critical electric field increases as η^0 approaches unity. It was also concluded that a stiffer structure will require a higher electric field to precipitate sling-shot buckling. Thus, the critical electric field is directly proportional to the length of the secondary layer, as well as the stiffness and thickness of this layer when compared to the primary layer of the structure.

A problem of this sort still has many aspects to still be researched. For example, the symmetric deformation assumption can be relaxed in order to consider antisymmetric deflections. Further, if non-symmetric deformations are considered, the secondary layer need not be centrally placed above the primary layer, which may result in drastically different behavior.

Delamination of the two layers is also something that can be considered. It is well known that delamination and buckling are not mutually exclusive phenomena, and in certain cases one often precipitates the other.

An experiment can be conducted to verify sling-shot buckling in a laboratory setting, and compared to the numerical simulations presented in this study. Since everything presented here is in non-dimensional form and a parameter study was included, the results apply for a wide range of materials.

References

[1] Bottega, W.J., 2006. Sling-shot buckling of composite structures under thermo-mechanical loading. Int. J. Mech. Sciences 48, 568-578.

[2] Bottega, W.J., Carabetta, P.M., 2009. On the detachment of patched panels under thermomechanical loading. J. Mech. of Materials and Structures 4, 1227-1250.

[3] Erturk, A., Inman, D.J., 2011. Piezoelectric Energy Harvesting. John Wiley & Sons Ltd, Chichester, United Kingdom.

[4] Karlsson, A.M., Bottega, W.J., 2000. On thermal buckling of patched beam-plates. Int. J. Solids Structures 37, 4655-4690.

[5] Karlsson, A.M., Bottega, W.J., 2000. On the behavior of a class of patched plates during cooling. Int. J. nonlinear Mech. 35, 543-566.

[6] Karlsson, A.M., Bottega, W.J., 2000. Thermo-mechanical response of patched plates. AIAA Journal 38, 1055-1062.

[7] Lanczos, C., 1986. The variational principles of mechanics. Dover Publication, Mineolay, New York, pp. 38-42.

[8] Leissa, A.W., 1987. A review of laminated composite plate buckling. Appl. Mech. Rev. 40, 575-591.

[9] Librescu, L., Souza, M.A., 1993. Post-buckling of geometrically imperfect shear-deformable flat panels under combined thermal and compressive edge loadings. J. Appl. Mech. 60, 526-533.

[10] Lippmann, G., 1881. "Principe de la conservation de l'lectricit" (in French). Annales de chimie et de physique 24: 145.

[11] Meressi, T., Paden, B., 1993. Buckling control of a flexible beam using piezoelectric actuators. Journal of Guidance, Control and Dynamics. 16, 977-980.

[12] Noor, A.K., Burton, W.S., 1992. Computational models for high-temperature multilayered composite plates and shells. Appl. Mech. Rev. 45, 419-446.

[13] Noor, A.K., Peters, J.M., 1992. Thermomechanical buckling of multilayered composite plates. J. Eng. Mech. 118, 351-366.

[14] Rutgerson, S.E., Bottega, W.J., 2002. Thermo-elastic buckling of layered shell segments. Int. J. Solids Structures 39, 4867-4887.

[15] Rutgerson, S.E., Bottega, W.J., 2004. Pre-Limit-Point Buckling of Multilayer Cylindrical Panels Under Pressure. AIAA Journal 42, 1272-1275.

[16] Stavsky, Y., 1975. Thermoelastic stability of laminated orthotropic circular plates. Acta Mechanica 22, 31-51.

[17] Sun, L.X., Hsu, T.R., 1990. Thermal buckling of laminated composite plates with transverse shear deformation. Comput. Struct. 36, 883-889.

[18] Tauchert, T.R., 1991. Thermally induced flexure, buckling, and vibration of plates. Appl. Mech. Rev. 44, 347-360.

[19] Thangaratnam, R.K., Palaninathan, R., Ramachandran, J., 1989. Thermal buckling of composite laminated plates. Comput. Struct. 32, 1117-1124.

[20] Thompson, S.P., Loughlan, J., 1995. The active buckling control of some composite column strips using piezoceramic actuators. Eighth Int. Conference of Composite Structures. 32, 59-67.

[21] Tierstan, H.F., 1969. Linear piezoelectric plate vibrations. Plenum Press, New York City, New York.

[22] Timoshenko, S., 1925. Analysis of bi-metal thermostats. J. Optical Society of America and Review of Scientific Instruments. 11, 233-255.

[23] Timoshenko, S., 1961. Theory of elastic stability. McGraw-Hill, New York City, New York.

[24] Varelis, D., Saravanos, D. A., 2004. Coupled buckling and postbuckling analysis of active laminated piezoelectric composite plates. Int. J. Solids Structures 41, 1519-1538.

[25] Wahl, A.M., 1944. Analysis of Valverde thermostat. J. Appl. Mech. 11, A183-A189.

[26] Yang, J., 2005. An introduction to the theory of piezoelectricity. Springer Science and Business Media, Inc., New York City, New York.